SOURCE CHARACTERIZATION OF SMALL TO MODERATE EARTHQUAKES IN THE EAST ANATOLIAN FAULT ZONE

by

Onur Batman

B.S., Civil Engineering, Kocaeli University, 2019

Submitted to the Kandilli Observatory and Earthquake Research Institute

In partial fulfillment of the requirements for the degree of

Master of Science

Graduate Program in Earthquake Engineering Department

Boğaziçi University

2025

SOURCE CHARACTERIZATION OF SMALL TO MODERATE EARTHQUAKES IN THE EAST ANATOLIAN FAULT ZONE

APPROVED BY:

Prof. Dr. Gülüm Tanırcan	…….
Prof. Dr. Ayşe Edinçliler	…….
Assist. Prof. Dr. Gökçe Tönük (MEF University)	…….

DATE OF APPROVAL: 10.01.2025



To Ilgaz Kemal,

ACKNOWLEDGEMENTS

As Gazi Mustafa Kemal said, "Those who set out not to rest never get tired." As someone who refuses to get tired in every aspect of my life, I would like to start by thanking Prof. Dr. Gülüm Tanırcan for his unwavering support, guidance, and enlightening presence during all the times I got tired during the thesis process, during the difficult moments, the unsolved problems and the times of exhaustion. As this long journey comes to an end, I would like to express my deepest gratitude for her care, dedication, and invaluable contributions. It was both an honor and a privilege to work under her guidance.

I am also deeply grateful to Prof. Dr. Ayşe Edinçliler, whose wisdom, advice, and guidance have shaped my research and academic journey since the start of my master's program. Her teachings and counsel will continue to inspire and guide me throughout my life.

I would like to express my gratitude to Assist. Prof. Dr. Gökçe, for his comments and feedback, significantly increased this thesis's academic rigor and depth.

I also owe a profound debt of gratitude to Prof. Dr. Seval Pınarbaşı Çuhadaroğlu for her support and unwavering belief in my potential. Her encouragement and influential words have been invaluable, both academically and personally. Without her mentorship, I would not have reached this stage or successfully completed this thesis.

I wish to express my appreciation to Prof. Dr. Ali Pınar, Prof. Dr. Eser Çaktı, Prof. Dr. Ufuk Hancılar, and Prof. Dr. Nuray Aydınoğlu for their invaluable knowledge and expertise, which greatly enriched my academic development during my graduate studies.

I owe everything to my family, whose unconditional love, unwavering belief, and boundless sacrifices have been my greatest source of strength and motivation. Even in the most challenging times, your faith in me was my greatest pillar of support. This thesis is as much your achievement as it is mine. My deepest thanks and love go to my father Ercan Batman, mother Nursen Batman, and sisters Gözde and Gizem Batman for their encouragement and inspiration every step of the way.

I would also like to express my gratitude to my Çırağan İnşaat, especially Mr. Adem İncesöz and Ms. Sibel İncesöz, for their unconditional support and trust in me.

Finally, I would like to thank my dear friends Berkin Atahan Gökbayrak, Serdar Çiçek, Hasan Talha Şahin, Fahrettin Kuran, and Abdullah Alkan, who were always there for me and supported me through every difficulty. Your companionship and encouragement have been a source of strength and inspiration.

ABSTRACT

SOURCE CHARACTERIZATION OF SMALL TO MODERATE EARTHQUAKES IN THE EAST ANATOLIAN FAULT ZONE

Source characterization of small to moderate shallow earthquakes in the East Anatolian Fault Zone (EAFZ) is studied through strong motion recordings in a broadband frequency range. Following the 2020 Mw 6.8 Sivrice earthquake in the Puturge segment of the EAFZ and the 2023 Pazarcik-Kahramanmaras and Ekinozu-Kahramanmaras earthquakes with moment magnitudes of Mw 7.7 and Mw 7.6, respectively, seismicity in the region has increased significantly. Source features such as strong motion generation areas (SMGA), stress drop, and rise time of 11 moderate-sized earthquakes ($5.0 < Mw < 6.8$) spanning a region from the Puturge segment to the Amanos segment have been determined using the Empirical Green's Function (EGF) Method.

Source parameter determination with simulations requires the optimal match between observed and simulated earthquake waveforms; however, there is a lack of consensus regarding the numerical expression for evaluating the adequacy of the fit in the EGF method. The best source parameters were identified by evaluating the average Goodness-of-Fit (GOF) based on nine different evaluation criteria, considering energy content and peak values, as well as frequency and time domain characteristics of the observed and simulated waveforms. The analyses revealed that stress drop in SMGA exhibits considerable variability, ranging from 0.75 to 22.3 MPa. It was found that small events at the southwestern tip of the Puturge segment released stress drops as high as those of moderate-size events, suggesting potential for future seismic activity.

Additionally, the study evaluated the consistency of the source parameters with global self-similar scaling relationships for earthquakes of different magnitudes. The calculated SMGA is smaller than rupture area estimations for smaller events. Conversely, SMGA for larger earthquakes closely follows the combined area of the asperity trend. For this reason, this study contributes to a new region-specific Mo-SMGA relationship for the EAFZ. The rise time derived from the simulations is consistent with global source relationships, indicating that the results conform to established global scaling laws.

ÖZET

DOĞU ANADOLU FAY HATTINDAKİ KÜÇÜK VE ORTA BÜYÜKLÜKTEKİ DEPREMLERİN KAYNAK ÖZELLİKLERİ

Doğu Anadolu Fay Hattı'ndaki (EAFZ) küçük ila orta büyüklükte sığ depremlerin kaynak karakterizasyonu, geniş bant frekans aralığında kuvvetli hareket kayıtları aracılığıyla incelenmiştir. EAFZ'nin Pütürge segmentindeki 2020 Mw 6.8 Sivrice depremi ve sırasıyla Mw 7.7 ve Mw 7.6 moment büyüklüklerine sahip 2023 Pazarcık-Kahramanmaraş ve Ekinözü-Kahramanmaraş depremlerinin ardından bölgedeki sismik aktivite önemli ölçüde artmıştır. Pütürge segmentinden Amanos segmentine kadar uzanan bir bölgeyi kapsayan 11 orta büyüklükteki depremin ($5.0 < Mw < 6.8$) kuvvetli hareket üretim alanları (SMGA), gerilim düşüşü ve yükselme zamanı gibi kaynak özellikleri Ampirik Green Fonksiyonu (EGF) Yöntemi kullanılarak belirlenmiştir.

Simülasyonlarla kaynak parametresi belirleme, gözlenen ve simüle edilen deprem dalga formları arasında iyi eşleşmeyi gerektirir. Ancak, EGF yönteminde uyumun yeterliliğini değerlendirmek için sayısal ifade konusunda bir fikir birliği yoktur. En iyi kaynak parametreleri, enerji içeriği ve tepe değerleri ile gözlenen ve simüle edilen dalga formlarının frekans ve zaman tanım alanı özelliklerini dikkate alarak dokuz farklı değerlendirme kriterine dayalı ortalama Uyum İyiliği (GOF) değerlendirilerek belirlenmiştir. Analizler, SMGA'daki stres düşüşünün 0,75 ila 22,3 MPa arasında değişen önemli bir değişkenlik gösterdiğini ortaya koymuştur. Pütürge segmentinin güneybatı ucundaki küçük depremlerin, orta büyüklükteki depremler kadar yüksek stres düşüşleri serbest bıraktığı bulunmuştur ve bu da gelecekte sismik aktivite potansiyeli olduğunu göstermektedir.

Ek olarak, çalışma kaynak parametrelerinin farklı büyüklükteki depremler için küresel ölçekleme ilişkileriyle tutarlılığını değerlendirmiştir. Hesaplanan SMGA, daha küçük depremler için kırılma alanı tahminlerinden daha küçüktür. Tersine, daha büyük depremler için SMGA, pürüzlülük eğiliminin birleşik alanını (combined area of asperity) yakından takip eder. Bu nedenle, bu çalışma EAFZ için bölgeye özgü yeni bir Mo-SMGA ilişkisine katkıda bulunulur. Simülasyonlardan türetilen yükselme süresi, küresel kaynak ilişkileriyle tutarlıdır ve bu da sonuçların yerleşik küresel ölçekleme yasalarına uyduğunu gösterir.

TABLE OF CONTENTS

ACKNOWLEDGEMENTS iv
ABSTRACT vi
ÖZET vii
LIST OF FIGURES xii
LIST OF TABLES xxiii
LIST OF SYMBOLS xxvii
LIST OF ACRONYMS/ABBREVIATIONS xxx
1. INTRODUCTION 1
1.1. Scope of Work 4
1.2. Literature Survey 5
1.2.1. East Anatolian Fault Zone (EAFZ) 5
1.2.1.1. Karliova Segment. 7
1.2.1.2. Ilica Segment. 7
1.2.1.3. Palu Segment. 8
1.2.1.4. Puturge Segment. 8
1.2.1.5. Erkenek Segment. 8
1.2.1.6. Pazarcik Segment. 9
1.2.1.7. Amanos Segment. 9
1.2.1.8. Seismicity of the EAFZ. 9
1.2.2. Emprical Green's Function (EGF) Method Applications 11
2. DATA USED IN THIS STUDY 19
2.1. Selection Criteria 21
2.1.1. Station Selection Criteria 21
2.1.1.1. Station Selection for Corner Frequency (fc) Estimation 21

2.1.1.2. Station Selection for EGF Method. 22
2.1.2. Earthquake Selection Criteria 24
2.2. Earthquake Couples 26
2.2.1. 24 January 2020 Mw 6.8 (1m) Sivrice and 19 March 2020 Mw 5.0 (1a) Malatya Earthquakes 26
2.2.2. 25 January 2020 Mw 5.1 (2m) Sivrice and 25 January 2020 Mw 4.4 (2a) Sivrice Earthquakes 28
2.2.3. 04 August 2020 Mw 5.6 (3m) Malatya and 04 August 2020 4.7 (3a) Malatya Earthquakes 31
2.2.4. 04 August 2020 Mw 5.6 (4m) and 11 February 2023 Mw 4.4 (4a) Malatya Earthquakes 32
2.2.5. 27 December 2020 Mw 5.6 (5m) and 17 January 2021 Mw 4.3 (5a) Elazig Earthquakes 34
2.2.6. 09 April 2022 Mw 5.2 (6m) Malatya and 09 April 2022 Mw 4.1 (6a) Malatya Earthquakes 37
2.2.7. 07 February 2023 Mw 5.4 (7m) and Mw 4.0 (7a) 07 February 2023 Adiyaman Earthquakes 38
2.2.8. 06 February 2023 Mw 5.3 (8m) and 07 February 2023 Mw 4.0 (8a) Kahramanmaras Earthquakes 40
2.2.9. 20 February 2023 Mw 6.3 (9m) and 07 February 2023 Mw 4.8 (9a) Hatay Earthquakes 42
2.2.10. 06 February 2023 Mw 5.8 (10m) Osmaniye and 09 February 2023 Mw 4.4 (10a) Gaziantep Earthquakes 43
2.2.11. 06 February 2023 Mw 6.7 (11m) Gaziantep and 26 August 2015 Mw 4.0 (11a) Kahramanmaras Earthquakes 45
3. METHOD of ANALYSIS 51
3.1. Brune Spectrum 51
3.1.1. Source Effects, *S (f)* 52
3.1.2. Path Effects, *P (f)* 53

3.1.3. Site Effects, *G (f)* 55
3.1.3.1. Amplification Factors, *AA (f)*. 56
3.1.3.2. Diminution Factors, *D (f)*. 56
3.2. Strong Ground Motion Simulation 58
3.2.1. Empirical Green's Function (EGF) Method 61
3.3. Evaluating Goodness-Of-Fit (GOF) Of Waveform 64
4. ANALYSES AND RESULTS 72
4.1. Corner Frequency (f_c) Estimation Results 72
4.2. Simulation Results 76
4.2.1. Blind EGF Simulation for 11th Eaarthquake Couple 82
4.2.1.1. Generating the artificial earthquake of Mw 5.0 with the 2015 Mw 4.0 Kahramanmaraş earthquake (11a). 82
4.2.1.2. Estimation of source parameters for the 2023 Mw 6.7 Gaziantep earthquake (11m) with the Mw 5.0 artificial earthquake 86
4.2.2. Stress Drop (Δσ) Results 88
5. DISCUSSION 91
5.1. Discussion of Goodness of Fit (GOF) Parameters 91
5.2. Discussion of Source Characterization for Broadband GM Simulation 94
5.3. Discussion of Stress Drop 99
6. CONCLUSIONS and SUGGESTIONS 105
6.1. Conclusions 105
6.2. Suggestions 107
REFERENCES 108
APPENDIX A: THE DETAILED BEST GOF TABLES AND GRAPHS 121
APPENDIX B: OBSERVED AND SYNTHETIC WAVEFORMS ACCORDING TO THE HIGHEST GOF PARAMETER 132

APPENDIX C: PGV COMPARISON FOR EGF SIMULATION 143

LIST OF FIGURES

Figure 1.1. The main fault systems of the plate boundaries [23]..... 6

Figure 1.2. Map of the East Anatolian strike-slip fault system showing strands, segments and fault jogs [23]. Abb: FS, fault Segment; (1) Duzici–Osmaniye fault segment; (2) Erzin fault segment; (3) Payas fault segment; (4) Yakapinar fault segment; (5) Cokak fault segment; (6) Islahiye REB; (7) Demrek RES; (8) Engizek fault zone; (9) Maras fault zone. 7

Figure 1.3. Distribution of both historical and instrumental earthquakes along the EAFZ [23], [34, 35], [39]. 10

Figure 2.1. Distribution of 11 earthquake couples and strong motion stations operated by AFAD along the EAFZ. Black stars denote the locations of mainshocks, yellow stars represent aftershocks, and blue triangles indicate the positions of strong motion stations. 20

Figure 2.2. The mainshock and aftershock from January 25, 2020, are depicted, with the black star indicating the mainshock and the yellow star representing the aftershock. Blue triangles denote the stations that recorded both seismic events. 25

Figure 2.3. The Mw 6.8 mainshock on January 24, 2020 and the Mw 5.0 aftershock on March 19, 2020 are depicted. The black and yellow stars represent the mainshock and aftershock, respectively. Blue triangles mark the stations that recorded both seismic events. 28

Figure 2.4. The Mw 5.1 mainshock and the Mw 4.4 aftershock on January 25, 2020 are depicted. The black and yellow stars represent the mainshock and aftershock, respectively. Blue triangles mark the stations that recorded both seismic events..... 29

Figure 2.5. Acceleration time history of the 2020 Mw 4.4 Sivrice aftershock that occurred on January 25, 2020, recorded at station 4404. 30

Figure 2.6. The Mw 5.6 mainshock and the Mw 4.7 aftershock on August 04, 2020 are depicted. The black and yellow stars represent the mainshock and aftershock, respectively. Blue triangles mark the stations that recorded both seismic events..... 32

Figure 2.7. The Mw 5.6 mainshock on August 04, 2020 and the Mw 4.4 aftershock on February 11, 2023 are depicted. The black and yellow stars represent the mainshock and aftershock, respectively. Blue triangles mark the stations that recorded both seismic events..... 34

Figure 2.8. A yellow star indicates the December 27, 2020 Mw 5.6 Elazig earthquake. (modified after Ramazan Demirtaş(2020))..... 35

Figure 2.9. The Mw 5.6 mainshock on December 27, 2020 and the Mw 4.3 aftershock on January 17, 2020 are depicted. The black and yellow stars represent the mainshock and aftershock, respectively. Blue triangles mark the stations that recorded both seismic events..... 36

Figure 2.10. The Mw 5.2 mainshock and the Mw 4.1 aftershock on April 09, 2022 are depicted. The black and yellow stars represent the mainshock and aftershock, respectively. Blue triangles mark the stations that recorded both seismic events..... 38

Figure 2.11. The Mw 5.4 mainshock and the Mw 4.0 aftershock on February 07, 2023 are depicted. The black and yellow stars represent the mainshock and aftershock, respectively. Blue triangles mark the stations that recorded both seismic events..... 40

Figure 2.12. The Mw 5.3 mainshock on February 06, 2023 and the Mw 4.0 aftershock on February 07, 2023 are depicted. The black and yellow stars represent the mainshock and aftershock, respectively. Blue triangles mark the stations that recorded both seismic events..... 41

Figure 2.13. The Mw 6.3 mainshock on February 20, 2023 and the Mw 4.8 foreshock on February 07, 2023 are depicted. The black and yellow stars represent the mainshock and aftershock, respectively. Blue triangles mark the stations that recorded both seismic events..... 43

Figure 2.14. The Mw 5.8 mainshock on February 06, 2023 and the Mw 4.4 aftershock on February 09, 2023 are depicted. The black and yellow stars represent the mainshock and aftershock, respectively. Blue triangles mark the stations that recorded both seismic events..... 45

Figure 2.15. The Mw 5.0 mainshock and the Mw 4.0 aftershock on August 26, 2015 are depicted. The black and yellow stars represent the mainshock and aftershock, respectively. Since the parameters of the small earthquake were used for both earthquakes, the black star and yellow star appear to be nested. Blue triangles mark the stations that recorded both seismic events..... 47

Figure 2.16. The Mw 6.7 mainshock on February 06, 2023 and the Mw 5.0 foreshock, are depicted. The black and yellow stars represent the mainshock and aftershock, respectively. Blue triangles mark the stations that recorded both seismic events..... 48

Figure 3.1. The displacement, velocity, and acceleration source spectra are modeled based on the omega-square (ω^{-2}) model (adapted from [70]). 52

Figure 3.2. a) The Filtering function, employed in the EGF method b) A schematic representation of the EGF method illustrates the fault dimensions of the large (L × W) and small (l × w) events. (Adapted from Houshmandviki et al. [48]) 63

Figure 4.1. For the Mw 6.3 mainshock of the 9th earthquake couple, the fc was estimated using both the acceleration and displacement FAS. The thick black lines represent the Brune spectrum. In this example, the f_c was identified as 0.68 Hz (see Table 4.1). The thick red line represents the logarithmic average calculated across all strong motion stations..... 74

Figure 4.2. Schematic representation of SMGA of the large earthquake simulated with the EGF method. ll x lw are the SMGA dimensions of the small events, respectively. The RSP of the main earthquake is represented by a red star. 77

Figure 4.3. Schematic representation of the Table 4.3. 79

Figure 4.4. Comparison between the PGV values found as a result of EGF simulations and the PGV values found from KTP24. 84

Figure 4.5. The residual values of PGV obtained from all Forward EGF simulations and KTP_24 GMPE [107] are illustrated using gray circles. Six models demonstrating the best fit were identified based on evaluating residuals across all stations. These selected models are distinguished by their respective color codes: red for Model 1, green

for Model 2, dark blue for Model 3, cyan for Model 4, purple for Model 5, and black for Model 6. 85

Figure 4.6. The schematic representation of SMGA and circular asperity model. 89

Figure 5.1. The average GOF value and the average GOF metrics were computed for each station across all 11 earthquake couples. 92

Figure 5.2. The bird's-eye view representation of the average GOF metrics calculated for each station. 93

Figure 5.3. Scaling of the Area - Mo relationship. The blue and gray lines, respectively, correspond to the RA and the combined area of asperities reported by Somerwille et al. [43]. The orange squares represent the SMGAs derived from the EGF simulations, while the purple crosses indicate the RAs theoretically estimated using the Wells and Coppersmith methodology [106]. 95

Figure 5.4. Scaling of the Area - Mo relationship from literature. The blue and gray lines, respectively, correspond to the RA and the combined area of asperities reported by Somerville et al. [43]. 96

Figure 5.5. Scaling co-seismic slip distribution of the 20 February 2023 Mw 6.3 Hatay earthquake obtained from finite-fault slip inversion with only teleseismic P- velocity data by Taymaz et al. [40]. The area shown with the black grid is the SMGA created according to the highest GOF value as a result of EGF simulations. The white star shows the RSP found after both waveform inversion and EGF simulations. 97

Figure 5.6. Scaling of the RT - Mo relationship from literature. The black line corresponds to the RT reported by Somerville et al. [43]..... 98

Figure 5.7. The stress drop values for 11 earthquake pairs occurring across various segments of the EAFZ are visually represented. 100

Figure 5.8. Distribution of stress drop values in segments on the EAFZ. 101

Figure 5.9. It is showing the inferred coseismic slip distribution during the 2020 Mw 6.8 Sivrice and 2023 Mw 7.7 Kahramanmaras earthquake (taken from Barbot et al. [109] and adapted). 102

Figure 5.10. Overview of stress drop results with other studies. 103

Figure A.1. Schematic representation of the detailed best GOF metrics for the 1st earthquake couple. 121

Figure A.2. Schematic representation of the detailed best GOF metrics for the 2nd earthquake couple. 122

Figure A.3. Schematic representation of the detailed best GOF metrics for the 3rd earthquake couple. 123

Figure A.4. Schematic representation of the detailed best GOF metrics for the 4th earthquake couple. 124

Figure A.5. Schematic representation of the detailed best GOF metrics for the 5th earthquake couple. 125

Figure A.6. Schematic representation of the detailed best GOF metrics for the 6th earthquake couple. 126

Figure A.7. Schematic representation of the detailed best GOF metrics for the 7th earthquake couple. 127

Figure A.8. Schematic representation of the detailed best GOF metrics for the 8th earthquake couple. 128

Figure A.9. Schematic representation of the detailed best GOF metrics for the 9th earthquake couple. 129

Figure A.10. Schematic representation of the detailed best GOF metrics for the 10th earthquake couple. 130

Figure A.11. Schematic representation of the detailed best GOF metrics for the 11th earthquake couple (mainshock Mw 6.7; aftershock Mw 5.0). 131

Figure B.1. Waveforms based on the highest GOF parameter in the EW direction for the Mw 6.8 Mainshock (1st earthquake couple). Black lines: observed records; red lines: synthetic records. 132

Figure B.2. Waveforms based on the highest GOF parameter in the NS direction for the Mw 6.8 Mainshock (1st earthquake couple). Black lines: observed records; red lines: synthetic records. 132

Figure B.3. Waveforms based on the highest GOF parameter in the EW direction for the Mw 5.1 Mainshock (2nd earthquake couple). Black lines: observed records; red lines: synthetic records. 133

Figure B.4. Waveforms based on the highest GOF parameter in the NS direction for the Mw 5.1 Mainshock (2nd earthquake couple). Black lines: observed records; red lines: synthetic records..... 133

Figure B.5. Waveforms based on the highest GOF parameter in the EW direction for the Mw 5.6 Mainshock (3rd earthquake couple). Black lines: observed records; red lines: synthetic records..... 134

Figure B.6. Waveforms based on the highest GOF parameter in the NS direction for the Mw 5.6 Mainshock (3rd earthquake couple). Black lines: observed records; red lines: synthetic records..... 134

Figure B.7. Waveforms based on the highest GOF parameter in the EW direction for the Mw 5.6 Mainshock (4th earthquake couple). Black lines: observed records; red lines: synthetic records..... 135

Figure B.8. Waveforms based on the highest GOF parameter in the NS direction for the Mw 5.6 Mainshock (4th earthquake couple). Black lines: observed records; red lines: synthetic records..... 135

Figure B.9. Waveforms based on the highest GOF parameter in the EW direction for the Mw 5.6 Mainshock (5th earthquake couple). Black lines: observed records; red lines: synthetic records..... 136

Figure B.10. Waveforms based on the highest GOF parameter in the NS direction for the Mw 5.6 Mainshock (5th earthquake couple). Black lines: observed records; red lines: synthetic records..... 136

Figure B.11. Waveforms based on the highest GOF parameter in the EW direction for the Mw 5.2 Mainshock (6th earthquake couple). Black lines: observed records; red lines: synthetic records..... 137

Figure B.12. Waveforms based on the highest GOF parameter in the NS direction for the Mw 5.2 Mainshock (6th earthquake couple). Black lines: observed records; red lines: synthetic records..... 137

Figure B.13. Waveforms based on the highest GOF parameter in the EW direction for the Mw 5.4 Mainshock (7th earthquake couple). Black lines: observed records; red lines: synthetic records..... 138

Figure B.14. Waveforms based on the highest GOF parameter in the NS direction for the Mw 5.4 Mainshock (7th earthquake couple). Black lines: observed records; red lines: synthetic records..... 138

Figure B.15. Waveforms based on the highest GOF parameter in the EW direction for the Mw 5.3 Mainshock (8th earthquake couple). Black lines: observed records; red lines: synthetic records..... 139

Figure B.16. Waveforms based on the highest GOF parameter in the NS direction for the Mw 5.3 Mainshock (8th earthquake couple). Black lines: observed records; red lines: synthetic records..... 139

Figure B.17. Waveforms based on the highest GOF parameter in the EW direction for the Mw 6.3 Mainshock (9th earthquake couple). Black lines: observed records; red lines: synthetic records..... 140

Figure B.18. Waveforms based on the highest GOF parameter in the NS direction for the Mw 6.3 Mainshock (9th earthquake couple). Black lines: observed records; red lines: synthetic records. 140

Figure B.19. Waveforms based on the highest GOF parameter in the EW direction for the Mw 5.8 Mainshock (10th earthquake couple). Black lines: observed records; red lines: synthetic records. 141

Figure B.20. Waveforms based on the highest GOF parameter in the NS direction for the Mw 5.8 Mainshock (10th earthquake couple). Black lines: observed records; red lines: synthetic records. 141

Figure B.21. Waveforms based on the highest GOF parameter in the EW direction for the Mw 6.7 Mainshock (11th earthquake couple). Upper panels: observed records; lower panels: synthetic records. Results of the 2023 MW 6.7 Gaziantep earthquake. 142

Figure B.22. Waveforms based on the highest GOF parameter in the NS direction for the Mw 6.7 Mainshock (11th earthquake couple). Upper panels: observed records; lower panels: synthetic records. Results of the 2023 MW 6.7 Gaziantep earthquake. 142

Figure C.1. Comparison of PGV according to simulated and KTP24 for the 1st model (N=2x3; C=2.6; ll x lw=1.8x1.0; RT=0.08; RSP=2x1). 143

Figure C.2. Comparison of PGV according to simulated and KTP24 for the 2nd model (N=3x2; C=2.6; ll x lw=1.0x1.2; RT=0.08; RSP=3x1). 144

Figure C.3. Comparison of PGV according to simulated and KTP24 for the 3rd model (N=3x2; C=2.6; ll x lw=0.8x1.4; RT=0.08; RSP=3x1). 144

Figure C.4. Comparison of PGV according to simulated and KTP24 for the 4th model (N=3x2; C=2.6; ll x lw=1.0x1.6; RT=0.08; RSP=3x1)..... 145

Figure C.5. Comparison of PGV according to simulated and KTP24 for the 5th model (N=3x2; C=2.6; ll x lw=1.0x1.8; RT=0.08; RSP=3x1)..... 145

Figure C.6. Comparison of PGV according to simulated and KTP24 for the 6th model (N=3x2; C=2.6; ll x lw=1.2x1.8; RT=0.08; RSP=3x1)..... 146

LIST OF TABLES

Table 2.1. The detailed information of the stations used in the EGF simulations and the fc estimations, are listed..... 23

Table 2.2. Characteristics of the Mw 6.8 Sivrice Earthquake on January 24, 2020 and the Mw 5.0 Malatya Earthquake on March 19, 2020. 27

Table 2.3. Characteristics of the Mw 5.1 Sivrice Earthquake and the Mw 4.4 Sivrice Earthquake on March 19, 2020. 29

Table 2.4. Earthquakes that occurred around 16:40 on January 25, 2020, in the Puturge segment from KOERI earthquake catalog. 30

Table 2.5. Characteristics of the Mw 5.6 Malatya Earthquake and the Mw 4.7 Malatya Earthquake on August 04, 2020. 31

Table 2.6. Characteristics of the Mw 5.6 Malatya Earthquake on August 04, 2020 and the Mw 4.4 Malatya Earthquake on February 11, 2023. 33

Table 2.7. Characteristics of the Mw 5.6 Elazig Earthquake on December 27, 2020 and the Mw 4.3 Elazig Earthquake on January 17, 2021. 35

Table 2.8. Characteristics of the Mw 5.2 Malatya Earthquake and the Mw 4.1 Malatya Earthquake on April 09, 2022. 37

Table 2.9. Characteristics of the Mw 5.4 Adiyaman Earthquake and the Mw 4.0 Adiyaman Earthquake on February 07, 2023. 39

Table 2.10. Characteristics of the Mw 5.3 Kahramanmaras Earthquake on February 06, 2023 and the Mw 4.0 Kahramanmaras Earthquake on February 07, 2023..... 41

Table 2.11. Characteristics of the Mw 6.3 Hatay Earthquake on February 20, 2023 and the Mw 4.8 Hatay Earthquake on February 07, 2023..... 42

Table 2.12. Characteristics of the Mw 5.8 Osmaniye Earthquake on February 06, 2023 and the Mw 4.0 Gaziantep Earthquake on February 09, 2023.. 44

Table 2.13. Characteristics of Mw 6.7 Gaziantep Earthquake on the February 06, 2023 and the Mw 4.0 Kahramanmaras Earthquake Augus 26, 2015.. 46

Table 2.14. Earthquake locations and parameters. 49

Table 4.1. Corner frequency (fc) estimation as a result of Spectral Analyses..... 75

Table 4.2. Initial parameters used in the simulation..... 76

Table 4.3. The distribution of the detailed best GOF metrics for the 2nd earthquake couple. 79

Table 4.4. The source parameters for the aftershock from forward EGF simulation. 80

Table 4.5. The source parameters for the mainshock from foward EGF simulation. 81

Table 4.6. The Preticted PGV values from KTP24. 83

Table 4.7. Source parameter models of Mw 5.0 earthquake calculated according to minimum residual values. 86

Table 4.8. Source parameters of Mw 4.0 and Mw 5.0 earthquakes. 87

Table 4.9. Source parameters of Mw 6.7 earthquake calculated according to highest GOF values. 88

Table 4.10. Estimated stress drop (Δσ) in the SMGA. 90

Table A.1. The distribution of the detailed best GOF metrics for the 1st earthquake couple. 121

Table A.2. The distribution of the detailed best GOF metrics for the 2nd earthquake couple. 122

Table A.3. The distribution of the detailed best GOF metrics for the 3rd earthquake couple. 123

Table A.4. The distribution of the detailed best GOF metrics for the 4th earthquake couple. 124

Table A.5. The distribution of the detailed best GOF metrics for the 5th earthquake couple. 125

Table A.6. The distribution of the detailed best GOF metrics for the 6th earthquake couple. 126

Table A.7. The distribution of the detailed best GOF metrics for the 7th earthquake couple. 127

Table A.8. The distribution of the detailed best GOF metrics for the 8th earthquake couple. 128

Table A.9. The distribution of the detailed best GOF metrics for the 9th earthquake couple. 129

Table A.10. The distribution of the detailed best GOF metrics for the 10th earthquake couple. 130

Table A.11. The distribution of the detailed best GOF metrics for the 11th earthquake couple (mainshock Mw 6.7; aftershock Mw 5.0). 131

LIST OF SYMBOLS

A (t) - a (t)	Observed acceleration waveform
A (f)	Observed acceleration spectrum
A_o - a_o	Constant level of the acceleration amplitude spectrum for the mainshock and aftershock, respectively
AA (f)	Amplification factor
D (f)	Diminution factor
D (t) - d (t)	Observed displacement waveform
G (t) - G (f)	Site amplification effect
G (R)	Geometrical spreading function
(f)	Frequecy
f_c	Corner frequency
f_{ca}	Corner frequency of the aftershock
f_{cm}	Corner frequency of the mainshock
$f_{cut\text{-}off}$	Cut-off frequency
F (t)	Filtering function
FAS	Fourier amplitude spectrum
f_{min}	The low-frequency cut-off
f_{max}	The high-frequency cut-off
FS	Free surface amplification factor
GOF	Goodness-of-fit
I_A	Arias intensity
IE	Energy integral
κ	Kappa factor
L - l	Length of SMGA for mainshock and aftershock, respectively
Mo	Sismik moment
Mw	Moment magnitude scale
Mb	Body-wave magnitude scale
Ms	Surface-wave magnitude scale
ML	Local (Richter) magnitude scale

n	The region's seismicity
n'	The shifting the artificial periodicity to a frequency range
P (t) - P (f)	Propagation path effect
PRTITN	The coefficient representing partition of S wave energy into two horizontal components
R , r	source to site distance
R_{epi}	Epicentral distance (km); distance from the epicenter to a specified site
R_{JB}	Joyner-Boore distance (km); closest distance to surface projection of rupture plane
R_{rup}	Rupture distance (km); closest distance to the ruptured plane
r_o	Distance from the site to the RSP
RSP	Rupture starting point
RT	Rise time
$R_{\theta\phi}$	Average radiation pattern for the S wave
S (t) - S (f)	Source effect
SA	Spectral acceleration
SNR	Signal-to-noise ratio
T	Rise time for the large event
Td	Total duration of strong ground motions
u (t)	Observed waveform for the small event
U (t)	Simulated waveform for the large event
U_o - u_o	Constant level of the displacement amplitude spectrum for the mainshock and aftershock, respectively
V (t) - v (t)	Observed velocity waveform
Vr	Rupture velocity
Vs	S-wave velocity
Vs30	Shear wave velocity of the top 30 m of the soil
W - w	Width of SMGA for mainshock and aftershock, respectively
Q (f)	Quality factor
ρ	Average crustal density
$\Delta\sigma$	Stress Drop
ω^{-2}	Omega-squared model

*	Convolution
ξ	Distance between the rupture starting point and the subfault

LIST OF ACRONYMS/ABBREVIATIONS

1a	Aftershock of the 1st earthquake couple
1m	Mainshock of the 1st earthquake couple
AFAD	Disaster and Emergency Management Authority
AF	African plate
AN	Anatolian microplate
AR	Arabian plate
C	Stress Drop scaling ratio
DSFZ	Dead Sea Fault Zone
DST	Deterministic simulation technique
E-	East
EAFZ	East Anatolian Fault Zone
EF	Ecemis fault
EGF	Empirical Green's function
EU	Eurasian plate
E-W	East-West
FC	Fault complexity
FS	Fault segment
GCMT	The Global CMT Project
GFZ	GeoForschungsZentrum Potsdam
GM	Ground motion
GOF	Goodnees of fit

HST	Hybrid/broadband simulation technique
KOERI	Kandilli Observatory and Earthquake Research Institute
Lat	Latitude
Long	Longitude
MED_RCMT	MedNet Regional Centroid Moment Tensors
MF	Malatya Fault
N-	North
N	Fault dimension scaling ratio
NAFZ	North Anatolian Fault Zone
NEIC	National Earthquake Information Center
N - S	North-South
PB	Paired bend
PGA	Peak Ground acceleration
PGD	Peak Ground displacement
PGV	Peak Ground velocities
PSA	Pseudo-spectral acceleration
RA	Rupture area
PB	Paired bend
REB	Releasing bend
RES	Releasing stepover
RSB	Restraining bend
RSDB	Restraining double bend
S-	South
SATZ	Southeast Anatolian Thrust Zone

SGM	Strong ground motion
SM	Strong Motion
SMGA	Strong Motion Generation Area
SSRF	Source Spectral Ratio Function
SST	Stochastic simulation technique
TF	Tuzgolu fault
USGS	United States Geological Survey
W-	West

1. INTRODUCTION

Throughout history, earthquakes have been among the most devastating natural disasters, causing destruction worldwide and impacting human lives and structures. The catastrophic effects of seismic events have led to significant damage across all types of structures, such as dams, bridges, and residential buildings, and resulting in the loss of thousands of lives. A multidisciplinary approach to examining earthquakes is essential to reduce the adverse effects of these natural disasters in geophysics engineering, earthquake engineering, urban planning, and disaster management. Understanding the dynamics and consequences of seismic events is critical for mitigating their impacts and enhancing disaster resilience.

An extensive comprehension of the mechanisms driving seismic events requires investigating the physical processes underlying earthquake ruptures. Among these, the analysis of earthquake source parameters is particularly significant, offering valuable knowledge of rupture dynamics and energy release. However, accurately determining these parameters remains challenging due to some limitations.

Key source parameters, such as fault rupture dimensions and stress differences, provide critical information about the physical properties of earthquake sources. Measuring the stress difference between the initial and final points of the earthquake has been instrumental in enhancing our understanding of the physics of the rupture process [1] and assessing seismic hazards [2]. However, although the stress difference, also known as stress drop ($\Delta\sigma$), can be determined easily from the corner frequency (f_c) of the Brune spectrum [3], the accuracy of these calculations is often compromised due to a lack of parameters or the use of averaged values in the equations.

Site effects should be taken into account when calculating $\Delta\sigma$ because they can lead to uncertainty of at least 30% [4]. However, it is pretty challenging to consider site effects in every earthquake-prone region. Additionally, various factors can complicate accurate assessments of source characteristics for earthquakes. These factors include a lack of knowledge about the ground conditions in the region where the earthquake occurred,

deficiencies in the soil layers and properties that the earthquake waves travel through before reaching the stations, and uncertainties in the data recorded at those stations. In such cases, ground motion simulations are a widely accepted and essential method for estimating source characteristics, as they incorporate detailed information about seismic parameters, earthquake physics, and faulting mechanisms.

Simulation techniques widely used when predicting strong ground motion can be classified into three types: (1) the deterministic simulation technique (DST) composed of numerical methods for wave propagation and Green's function method [5-7]; (2) the stochastic simulation technique (SST) comprises the point source method and finite fault method [8]; (3) the hybrid/broadband simulation technique (HST) by using DTS and SST together.

Green's functions for low-frequency ground motions (GM) are typically calculated using a deterministic approach, which relies on the consistent summation of rays or wave numbers. In contrast, high-frequency GMs are computed using a statistical approach based on random summation. Consequently, reproducing Green's functions within the intermediate frequency range of 0.5–2.0 Hz presents a significant challenge. In addition to that, high frequency simulations necessitate local amplification spectra of sites of interest.

The Empirical Green's Function (EGF) method, developed by Irikura, provides a framework for characterizing near-source strong ground motion (SGM) across a broad frequency range, particularly between 0.01 and 10 Hz [9]. The key advantage of the EGF method over other methods is that propagation and site response characteristics are implicitly used in the simulation through the usage of recorded motions as Green's function. As a result, the EGF method is widely preferred for simulating strong ground motions.

In Turkiye, earthquakes with a magnitude of 5.0 to 5.9 occur approximately every 48 days, while those with a magnitude of 6.0 to 6.9 take place every 17 months. The most destructive earthquakes, magnitudes of 7.0 or greater, occur every 6.2 years between 1900 and December 31, 2024 [10]. Given Turkiye's high seismic activity, it is crucial to analyze past earthquakes to inform future mitigation strategies accurately. These analyses are essential for implementing regulations aimed at minimizing the impact of earthquakes, conducting site-specific assessments based on local geological conditions, and performing

comprehensive hazard analyses. Furthermore, the results can be used to develop key parameters for sectors such as insurance, where earthquake risk is a critical factor.

East Anatolian Fault Zone (EAFZ) and North Anatolian Fault Zone (NAFZ) are two of the most significant fault lines responsible for generating major earthquakes in Turkiye. The NAFZ, in particular, passes through highly developed urban areas such as Istanbul and Kocaeli, where extensive seismic stations have been established, and the geotechnical properties of these sites have been thoroughly assessed. In contrast, monitoring in the country's eastern regions, along the EAFZ, faces considerable challenges. Until the last two decades, adverse weather conditions, geographic difficulties, and limited internet access have restricted the number of seismic stations in this area. Furthermore, the lack of information regarding the ground conditions at recording sites impedes the accurate determination of earthquake source parameters.

Despite significant earthquakes in the EAFZ over the past 50 years, including the 1971 Bingol (Ms 6.9), 1975 Lice (Ms 6.7), 1992 Erzincan (Mw 6.7), 2003 Bingol (Mw 6.3), and 2010 Elazig (Mw 6.1) events, earthquake records remain limited. However, technological advancements have enabled more comprehensive measurements of the 2020 Sivrice earthquake (Mw 6.8) and its aftershocks.

The limited availability of earthquake records prior to the 2020 Sivrice (Mw 6.8) earthquake prevent comprehensive research in the region. However, the precise recording of seismic events following the last decade, together with a comprehensive understanding of the ground properties where the earthquakes are measured, have significantly increased prediction capabilities.

The subject of this thesis was initiated in 2022, considering the seismic silence in the segments on the EAFZ. The primary objective is to investigate the source characteristics of the available intermediate-size earthquakes in the fault segments of the EAFZ. The quantity of significant data in the region increased following the Kahramanmaras earthquake sequence (Mw 7.7 and Mw 7.6), which occurred on February 6, 2023. This influx of data enables the investigation of earthquake source parameters in other segments of the EAFZ. Therefore, the identified source parameters are analyzed to assess their relationship with the fault segments and are also further compared to global source scaling relationships.

The objectives of this study are:

- Ground motion simulation of the 11 ($5.0 \leq Mw \leq 6.8$) main events using 11 ($4.0 \leq Mw \leq 5.0$) small events by the EGF Method in a broad frequency range.
- Investigation on variabilities of mainshock/small shock stress drop ratio at different segments of EAFZ.
- Comparison of the derived source parameters with global source scaling relationships.
- Development of an empirical equation to estimate Strong Motion Generation Areas (SMGA) for intermediate-size earthquakes.

1.1. Scope of Work

- Previous studies on the EGF method and Turkiye's tectonic are presented in Chapter 1.
- The selection criteria for earthquake records, the methods for choosing these records, and the stations utilized for analysis are detailed in Chapter 2.
- Chapter 3 provides an overview of the methods employed in the study. It begins with a description of the data processing techniques used to determine the corner frequencies of the seismic events. This is followed by an explanation of the EGF method, which is utilized to identify the source characteristics of earthquake pairs. Lastly, the section outlines the parameters used to evaluate the accuracy of the EGF results and elaborates on their significance.
- Chapter 4 presents the findings on the source properties determined using the EGF method.
- These results are compared with global source scaling relationships and previous research for validation and context in Chapter 5.
- The conclusions drawn from the study and the recommendations for future research directions are provided in Chapter 6.

1.2. Literature Survey

1.2.1. East Anatolian Fault Zone (EAFZ)

Over the past four years, the eastern part of Turkiye has experienced three notable earthquakes: the 2020 Sivrice (Mw 6.8) earthquake and the 2023 Kahramanmaras (Mw 7.7 and Mw 7.6) earthquakes. While these events originate along the EAFZ, their impacts are widespread, affecting many regions within Turkiye and neighboring countries, including Iran, Iraq, and Syria. For this reason, Turkiye's tectonic dynamics need to be well understood.

It can be briefly expressed that the seismic activity of the East Anatolian region is primarily driven by the continuous movement of the Eurasian, African, and Arabian plates [11-18]. The Arabian plate is moving in a north-northeast direction relative to Eurasia at a rate of approximately 15 mm/year. This ongoing northward migration leads to continental collision along the Bitlis Suture Zone [19-21]. Meanwhile, the northward motion of the African plate results in the subduction of the oceanic lithosphere beneath the Anatolian plate along the Aegean-Cyprian Arc [19], [22].

As a result of these tectonic movements, Turkiye can be divided into three primary seismotectonic regions, each with distinct patterns of earthquake activity, as illustrated in Figure 1.1. These regions include (1) the northern and northwestern areas, which are dominated by strike-slip faulting along the NAFZ; (2) the eastern region, characterized by strike-slip deformation along the EAFZ; and (3) The Aegean region, where north-south extensional tectonics are dominant and where normal and oblique faulting are generally present [24-27].

Among these, the EAFZ is quite complex, consisting of parallel and sub-parallel left-lateral strike-slip and oblique faults. These faults are segmented based on changes in fault orientation and offsets, with relative motion velocities between the Arabian and Anatolian plates ranging from 4–5 mm/year in the south-west to approximately 10 mm/year in the north-east [28-32]. Plate motions and the regional tectonic dynamics are illustrated in Figure 1.1.

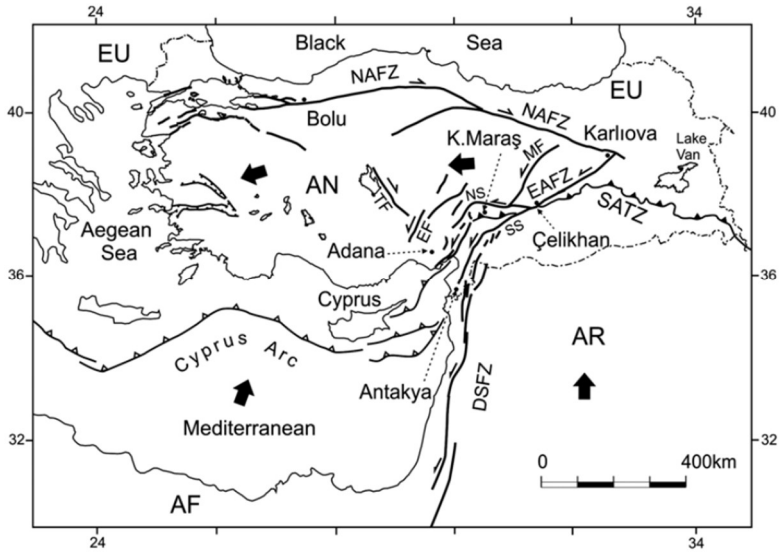


Figure 1.1. The main fault systems of the plate boundaries [23]

Abb: AN, Anatolian microplate; AF, African plate; AR, Arabian plate; EU, Eurasian plate; DSFZ, Dead Sea Fault Zone; MF; Malatya Fault, TF, Tuzgolu fault; EF, Ecemis fault; SATZ, Southeast Anatolian Thrust Zone; SS, southern strand of the EAFZ; NS, northern strand of the EAFZ.

Fault strands are generally divided into segments based on fault jogs, which include extensional and compressional geometric complexities like stepovers and bends. The EAFZ features several notable fault jogs, including the Goynuk paired bend (PB), Gokdere restraining bend (RSB), Lake Hazar releasing bend (REB), Yarpuzlu restraining double bend (RSDB), Golbasi releasing stepover (RES), Turkoglu releasing bend (REB), Nurhak fault complexity (FC), Goksun releasing bend (REB), and Delihalil releasing stepover (RES). At the same time, these jogs create variations in fault orientation [23].

One of the most recent studies on segmentation along the EAFZ is presented by Duman and Emre [23] based on field observations, and it is stated that the EAFZ consists of two main branches, south and north. The southern strand represents the primary fault strand (see Figure 1.2), delineating a roughly 580-km-long plate boundary between Karliova and Antakya. Considering fault jogs, the main branch is composed of several fault segments, including the Karliova (31 km), Ilica (40 km), Palu (77 km), Puturge (96 km), Erkenek (62 km), Pazarcik (82 km), and Amanos (112 km) segments. The northern strand includes the

Surgu (55 km), Cardak (85 km), Savrun-Cokak-Toprakkale (137 km) and Yumurtalik-Karatas-Yakapinar-Duzici-Iskenderun (240 km) segments. On the fault map, the Surgu Fault branches off from the main fault near Celikhan and extends approximately 30 km westward.

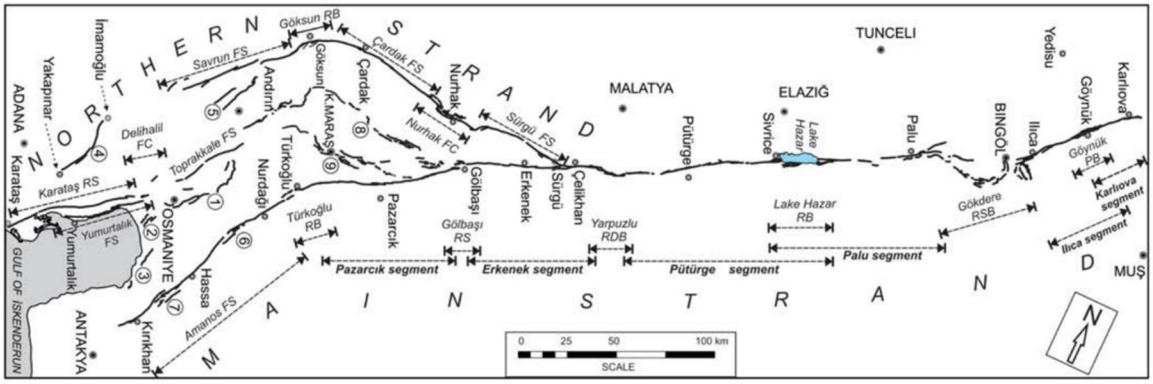


Figure 1.2. Map of the East Anatolian strike-slip fault system showing strands, segments and fault jogs [23]. Abb: FS, fault Segment; (1) Duzici–Osmaniye fault segment; (2) Erzin fault segment; (3) Payas fault segment; (4) Yakapinar fault segment; (5) Cokak fault segment; (6) Islahiye REB; (7) Demrek RES; (8) Engizek fault zone; (9) Maras fault zone.

1.2.1.1. Karliova Segment.

The Karliova Segment originates at the convergence of the NAFZ and the EAFZ along the eastern boundary of the Karliova basin. This basin, recognized as the Karliova Triple Junction, is a significant tectonic feature due to the intricate interactions between the NAFZ and EAFZ [32, 33]. Characterized by active left-lateral strike-slip faulting, the Karliova Segment links to the Ilica Segment through the Goynuk PB, a structure approximately 16.5 km in length.

1.2.1.2. Ilica Segment.

The Ilica Segment is defined by a single that follows along the Goynuk River valley. The 1971 Bingol earthquake (Ms 6.8) highlights the segment's seismic significance, which occurred along the EAF between Karliova and Bingol [11]. The Ilica Segment is characterized by left-lateral strike-slip faulting. Initially, the Karliova and Ilica segments were classified as a single segment of the EAFZ. However, it was later observed that faulting

features in the Karliova Segment do not extend toward the Goynuk fold. Consequently, this fault is now divided into two distinct segments, joined by the Goynuk double fold. Finally, the approximately 45 km long Gokdere RSB connects the Ilica and Palu sections.

1.2.1.3. Palu Segment.

The Palu Segment is located between the Gokdere RSB to the northeast and the Lake Hazar REB to the southwest, forming the largest jog structures along the EAF. The western part of this segment, approximately 40 km long, extends from the Keban Dam reservoir to Lake Hazar. While the segment predominantly displays left-lateral, strike-slip fault characteristics, some branches also exhibit normal dip-slip fault structures. The most recent significant earthquake along this segment (Ms 7.1) occurred on May 3, 1874 [34, 35], and historical records indicate that it caused considerable damage in the area between Lake Hazar and Palu. Additionally, the Puturge and Palu segments encompass the 10-km-long Lake Hazar REB.

1.2.1.4. Puturge Segment.

The Puturge Segment extends from the Lake Hazar REB to the Yarpuzlu RSDB. Significant left-lateral offsets have been recorded along this segment, indicative of active strike-slip movement that aligns with the dominant motion of the EAFZ. The Puturge segment has a history of significant seismic events, producing the 1875 (Ms 6.7) and 1905 (Ms 6.8) earthquakes [34]. The 2020 Sivrice earthquake (Mw 6.8) further highlights the segment's potential for significant seismic events [36]. The 2020 Sivrice (Mw 6.8) earthquake has resulted in extensive structural and non-structural damage across the affected region.

1.2.1.5. Erkenek Segment.

The Erkenek Segment connects to a 15 km-long double restraining bend at its eastern end at Yarpuzlu, linking it to the Puturge Segment. Characterized by active left-lateral strike-slip faulting, the Erkenek Segment extends southwestward towards the Golbasi RES. The Golbasi RES, which is approximately 4 km long, adds additional complexity to the segment.

The most recent major earthquake recorded in this segment is likely the 1893 event (Ms 7.2) [34, 35].

1.2.1.6. Pazarcik Segment.

The Pazarcik Segment extends from the Golbasi RES to the Turkoglu REB. There are observable left-lateral offsets along the length of this line, indicating a left-lateral strike-slip faulting characteristic of the EAFZ. The Turkoglu REB spans approximately 8 km in length. As a result of paleoseismological studies, it is thought that the surface ruptures in this segment are the result of the 1114 and 1513 earthquakes [23].

1.2.1.7. Amanos Segment.

The Amanos Segment of the EAFZ consists of three main segments: the Nurdagi, Hassa, and Kirikhan segments.

The Nurdagi segment, approximately 40 km long, initiates at the Turkoglu RES and connects to the Islahiye REB at its southern end. While left-lateral strike-slip faulting characterizes the Nurdagi segment, oblique normal faults are also observed in this section. Similarly, the east and west coasts of the 15 km long Islahiye REB are predominantly bounded by oblique normal faults.

The 45 km-long Hassa segment extends from the Islahiye bend to the Demrek RES. Left-lateral faulting is commonly observed along the Hassa segment and in the vicinity of the Demrek RES [37].

The Kirikhan segment, beginning near the midpoint of the 15-km Demrek RES, displays a concave fault geometry with active left-lateral faulting. It is recorded that a significant earthquake (M 7.5) occurred near the Amanos branches in 1822, causing a 200 km-long rupture [35], [38].

1.2.1.8. Seismicity of the EAFZ.

EAFZ has a long and active seismic history punctuated by numerous earthquakes, some of which are shown in Figure 1.3. According to the statement made by KOERI, the

Nurdagi-Pazarcik and the Mw 7.6 Ekinozu-Elbistan events on February 6, 2023, represented the largest seismic occurrences in Turkey since 1939 and are located in the Pazarcik and Surgu-Cardak segments of the EAFZ, respectively. Following these 2023 Kahramanmaras earthquakes, multiple moderate to large aftershocks with moment magnitudes above six have been recorded.

Firstly, it is the largest aftershock with a magnitude of Mw 6.7 that occurred shortly after the February 6, 2023, Mw 7.7 Pazarcik earthquake. According to USGS, it occurred southwest of the epicenter of the Mw 7.7 Nurdagi-Pazarcik earthquake.

Secondly, two weeks after the Kahramanmaras earthquakes, on February 20, 2023, a moderate aftershock with a magnitude of Mw 6.3 occurred near the southwestern edge of Defne. This earthquake has been strongly felt in Hatay and its surrounding areas, causing significant damage near the epicenter. Various institutions characterize the 2023 Mw 6.3 Defne earthquake as a normal faulting mechanism with a left-lateral strike-slip component. Taymaz et al. [40] aim to reveal the source of the earthquake and the rupture characteristics. The rupture extends over a fault line approximately 36 km in length and 15 km in width, covering an area of roughly 540 km². Moment magnitude estimates for the event ranged from 6.2 to 6.4, depending on the modeling method used. According to Kanamori and Anderson [41], interplate earthquakes tend to have low stress drops, and the stress change in the 2023 Mw 6.3 Defne earthquake has been calculated to be between 3 and 7 bar, which is consistent with this observation.

1.2.2. Emprical Green's Function (EGF) Method Applications

One of the most effective methods for simulating broadband strong ground motions generated by a large earthquake is to use observed records from small earthquakes occurring around the source area of a large earthquake.

The EGF method operates on the premise that GM records from small earthquakes occurring in proximity to the fault of a larger earthquake can be leveraged as Green's functions to estimate the ground motion of the larger event. These small-event GMs, referred to as Green's functions, are superposed to estimate the GM of a large earthquake. The main advantage of the method is that the GM can be estimated accurately without explicitly

evaluating the path and site effects because those effects are naturally included in the record of the GM of a small event.

For the validity of this approach, all subevents must have focal mechanisms similar to that of the simulated main event. Additionally, the epicenters of the small and large events must be spatially close to ensure consistency. That is, the EGF approach treats small earthquakes as point-source Green's functions under the assumption that the focal mechanisms, propagation paths, and site effects of the small and large earthquakes are identical.

SMGAs, which reproduce near-source GMs over a broadband frequency range, are typically estimated using the EGF technique. SMGAs are defined as localized regions within the total rupture area (RA) that exhibit relatively high slip velocities [42]. The estimation of SMGAs involves waveform fitting using the EGF method, where the source model assumes homogeneous slip distribution and uniform rise time (RT), with radial rupture propagation initiating from the rupture point.

Typically, SMGAs are smaller than the total RAs obtained through waveform inversion analyses. Somerville et al. have found that the effective source area responsible for strong ground motions constitutes approximately one-quarter of the total RA determined through low-frequency waveform inversions [43]. Despite this smaller size, the GMs produced by SMGAs are nearly identical to those produced by a characterized source model in terms of acceleration and velocity [42-44]. In addition, the influence of the background slip area on the waveform is very minimal [42].

In conclusion, SMGAs derived from EGF analyses represent a valuable tool for estimating earthquake source parameters and understanding the mechanism of strong ground motion generation. Numerous studies have employed the EGF method to estimate SMGAs by simulating the GMs of target earthquakes.

The EGF method, first introduced by Hartzell [7] in 1978, has been extensively developed and proposed by researchers such as Hutchings [45] and Irikura [9]. While both approaches utilize observed small earthquake records to simulate the GMs of larger events, they differ in methodology and application.

Hutchings' method [45] emphasizes the "prediction" of GMs through the systematic superposition of Green's functions using a stochastic framework. This approach incorporates

randomness in the rupture process, making it particularly suitable for scenarios requiring high variability or accommodating uncertainties in modeling.

Conversely, Irikura's method [9] adopts a deterministic approach, focusing on accurately scaling and summing small-event records to replicate the rupture characteristics of larger earthquakes. This approach introduces scaling parameters N and C, which relate small and large events based on stress drops, fault dimensions, and slip velocity time functions. The fault plane is divided into subfaults, with aftershock records used as Green's functions for each subfault. This method is especially effective for simulating precise, near-source ground motions.

In this study, the methodology developed by Irikura [9] was selected and employed to estimate strong ground motions and derive source parameters, owing to its reliability and precision in near-field simulations.

One of the pioneering studies on EGF simulation has been performed by Hartzell [7]. This study presents an important methodology for modeling strong ground motions using aftershocks as Green's functions. The approach assumes a large earthquake as a collection of discrete point sources distributed across the fault plane. Accurate modeling requires aftershocks to provide adequate azimuthal coverage of the fault. Additionally, aftershock GM recordings must be recorded from the same strong motion stations as the mainshock to ensure consistency in path and site effects. Similarly, this method assumes similarity in focal mechanisms between the mainshock and aftershocks. The mainshock's GM is reconstructed by summing the scaled and temporally shifted responses from aftershock records. Hartzell successfully applied this method to the 1940 Imperial Valley earthquake. The resulting synthetic waveforms closely matched observed GMs, demonstrating the efficacy of this approach in capturing complex, long-duration near-field seismic events.

Irikura [9] investigates the scaling laws of seismic spectra by analyzing spectral ratios from earthquake pairs with comparable epicenters but differing magnitudes. The spectral characteristics of smaller earthquakes ($Mw < 6.1$) conform to the omega-squared (ω^{-2}) model. However, larger events (Mw 7.1 and Mw 7.7) display enhanced high-frequency components that deviate from the ω^{-2} model and are better represented by the revised model, which incorporates parameters such as crack size and the number of cracks. A novel method for synthesizing strong ground motions using the EGF technique is introduced. In this

approach, the fault plane of a large earthquake is divided into smaller elements matching the fault dimensions of a smaller earthquake, which serves as Green's function. The GM for the larger event is synthesized by summing and temporally shifting the smaller event's records to replicate the rupture propagation over the fault plane. The revised model ensures the synthetic motions align with the ω^{-2} model when both the large and small earthquake spectra adhere to this scaling. This method also incorporates high-frequency spectral contributions, making it suitable for simulating large earthquake motions across broad frequency ranges. This methodology underscores the significance of stress drop and fault dimension parameters in achieving spectral consistency with observed ground motions.

Miyake et al. [42] investigate the source models of 12 crustal earthquakes with moment magnitudes ranging from 4.8 to 6.5, which occurred in Japan between 1996 and 1999. These earthquakes are analyzed using the EGF method formulated by Irikura [9]. The source models for the main events are constructed by analyzing records from stations within 50 km of the epicenters. The study defines the SMGA as an extended zone characterized by large slip velocities within the RA. Best source model parameters like the SMGA and RT are estimated, minimizing residuals between observed and synthetic waveforms. While the synthetic waveforms generated from the source models fit the observed data well regarding acceleration and velocity, some discrepancies are noted in the displacement amplitudes. On the other hand, at low frequencies, Miyake et al. make comparisons with previous research on slip heterogeneity in these crustal earthquakes [43], [46, 47]. By using Somerwille's work [43], they analyze heterogeneous slip distributions from waveform inversions in the 0.1–0.5 Hz frequency range for the earthquakes, revealing that asperities (regions of large slip) correlate with the SMGA, suggesting that occupying almost the same regions. SMGA is close to the combined area of asperities [43] and shows the best-fitting acceleration and velocity waveforms for forward modeling. Lastly, for broadband GM simulations, the authors propose a characterized source model that includes an SMGA with large slip velocity and a background slip area with smaller slip velocities. The slip velocity-time function shows that SMGA sub-faults exhibited larger slip velocities but shorter durations than background slip areas. This result confirms that the near-source ground motions are predominantly influenced by the size and rise time of the SMGA, indicating that both high- and low-frequency components of the GM are controlled by the SMGA dynamics.

In the Mw 6.1 earthquake near Parkfield, California, the source modeling utilizes the EGF method to characterize near-source strong ground motion within a broadband frequency range [48]. The SMGA obtained from the EGF, identified as having uniform slip with a high slip velocity, is particularly effective in reproducing near-source ground motions. Four medium-magnitude earthquakes, namely 2005 (Mw 4.5), 2007 (Mw 4.0), 2010 (Mw 4.0), and 2012 (Mw 4.4), are selected as Green's functions due to their proximity to the epicenter and the similarity of their focal mechanisms with the mainshocks. Then, the SMGA obtained from the EGF is compared with the asperities derived from the inversion of the waveform. Custodio et al. [49] employ non-linear global inversion to develop a slip model that reveals two primary slip area concentrations on the fault surface. Similarly, Ji [50] applies low-frequency waveform inversion to identify heterogeneous slip distributions and detect two distinct slip patches. Ground motion simulations using the characterized source model obtained from waveform inversion, such as Custodio et al. [49] and Ji [50], exhibit better agreement with the observed records compared to the single SMGA models obtained from the EGF method, especially for acceleration and velocity. However, this improvement does not apply to the displacement waveform. On the other hand, observed and synthetic results are compared regarding the pseudo acceleration (PSA) response spectra considering a 5% damped oscillatory. The characterized source models and single SMGA models performed well in the 0.1–2.0 Hz frequency range, though the single SMGA models give better results between 2.0–10.0 Hz. So, it is necessary to use EGF in broadband simulations. Lastly, the analysis indicates that the directivity of fault rupture plays a critical role in influencing the spectral amplitude of the observed GMs.

The 2016 Mw 7.0 Kumamoto earthquake, one of the most critical seismic events in Japan since the 1995 Hyogo-ken Nambu earthquake, is a case for evaluating the applicability of established source scaling relationships for crustal earthquakes in Japan [51]. Initially, rupture and asperity areas are identified based on slip distributions obtained from waveform inversions within the 0.05-1 Hz frequency range [52-54]. Yoshida et al. [52] propose a more complex fault model, incorporating four fault segments with distinct strike and dip angles, while Kubo et al. [54] assume a single fault plane in their waveform inversion. Subsequently, the GMs of the Kumamoto earthquake are simulated based on the EGF method, utilizing a characterized source model of SMGAs. Two characterized source models are referenced to determine the source parameters for EGF: the first is multiple SMGAs derived from their slip distribution model based on Yoshida et al. [52], while the second is a single SMGA

derived from their slip distribution model based on Kubo et al. [54]. In Yoshida's model, the fit between synthetic and observed waveforms is assessed through visual inspection, whereas Kubo's model employed residual minimization between synthetic and observed waveforms [55]. Despite differing modeling approaches, both studies reach similar conclusions. The combined area of the three SMGAs from Yoshida's model and the single SMGA from Kubo's model produced by EGF are found to be nearly identical in terms of location and size. Moreover, the synthetic GMs for acceleration, velocity, and displacement produced by both models exhibit the same amplitudes, further validating the effectiveness of these forward modeling approaches in reproducing the observed seismic data.

Irikura and Miyake [56] present a methodology for predicting strong ground motions based on a characterization of the seismic source model and the application of EGF for future earthquake scenarios. The source model is defined by three critical types of parameters: (1) outer fault parameters, representing the total RA and seismic moment (M_o); (2) inner fault parameters, which include the area of asperities and their $\Delta\sigma$s; and (3) extra fault parameters, which account for the rupture starting point (RSP) and propagation pattern. Accuracy of the source model characterized by the prescription is provided by comparing the Peak Ground Velocities (PGV) of the simulated GMs with PGVs derived from empirical attenuation relationships. On the other hand, the validity and applicability of the model are investigated by comparing simulated and observed GMs for the 1995 Kobe [57] and 2005 Fukuoka [58] earthquakes, whose source parameters are known from the waveform inversion. The results demonstrate a high degree of harmony between the observed and synthetic waveforms of PGVs, highlighting the model's effectiveness in accurately predicting strong ground motions.

Birgoren et al. [59] analyzed the rupture process of the 1999 Duzce Earthquake using waveform inversion and EGF simulations. Low-frequency ground motions (0.1–0.5 Hz) were investigated through multi-time-window linear waveform inversion to determine slip distributions and locate asperities. Additionally, high-frequency GMs (0.3–10 Hz) were modeled using the EGF method to image SMGAs. The analysis identified two distinct asperities: a larger asperity near the hypocenter and a smaller one situated closer to the surface on the eastern fault plane. Rupture velocities (Vr) were determined to be approximately 2.9 km/s in the western fault plane and between 3.5–3.6 km/s in the eastern segment. Notably, the eastward propagation of the rupture within the large asperity partially

exceeded the S-wave velocity (Vs) in the eastern region, reaching values as high as 4.7 km/s. These findings suggest that while most of the rupture propagated at velocities near the S-wave speed, localized supershear behavior occurred during the eastern propagation. Results from EGF simulations further validated these observations, showing rupture velocities in the eastern SMGA consistent with near S-wave speeds.

Tanircan and Savas [60] focus on modeling scenario-based strong ground motion distribution in the Yalova-Bursa region, emphasizing near-field effects such as source characteristics and rupture propagation (directivity). Employing Irikura's EGF method [9], the study simulated an Mw 4.8 earthquake using an Mw 3.3 event as the Green's function. The source parameters derived from the Mw 4.8 simulation were subsequently utilized to model the Mw 6.9 scenario earthquake in Gemlik Bay, assuming a 40 km rupture along the fault segment. Simulations for three distinct rupture scenarios were evaluated regarding acceleration, velocity, and spectral response data. The results highlight that asperity and hypocenter locations are critical factors influencing strong ground motion. GM amplitudes, especially peak ground acceleration (PGA), are significantly affected by stress drop ratios (C), with higher stress drop ratios leading to increased PGA and PGV. Variability in $\Delta\sigma$ assumptions may produce different GM amplitudes. Lastly, Tanircan and Savas's study focuses on modeling one of the region's worst-case earthquake scenarios and emphasizes the need for future research on deterministic rupture scenarios to estimate damage and losses effectively.

Baykal et al. [61] utilized the EGF method to simulate the strong ground motion of the 2010 Elazig Kovancilar Earthquake (Mw 6.1) and its largest aftershock (Mw 5.5) by employing records of a smaller earthquake (Mw 4.8) as the Green's function. Source models were developed for both the mainshock and the aftershock, with the fitting quality between observed and synthesized motions verified through visual inspection. The results were compared to the scaling relationship of SMGA to M_o proposed by Miyake et al. [42]. While the SMGA of the largest aftershock aligned well with Miyake's scaling, the mainshock exhibited a relatively larger M_o, deviating from the scaling relationship. The mainshock generated seismic moments from a smaller portion of the fault plane at a focal depth of 5 km, which may explain the significant destruction caused by the event. Additionally, the aftershock's RT within the SMGA was consistent with the empirical scaling relationship, whereas the mainshock's RT was shorter than expected. The analysis also revealed that the

stress drop scaling factor (C) for the SMGA of the mainshock was 1.4 times higher than that of the largest aftershock, reflecting distinct source characteristics between the two events.

Tanircan et al. [62] examine the variability of $\Delta\sigma$ in shallow normal-faulting earthquakes within the Aegean region through the application of near-source ground motion simulations. The investigation focuses on three significant events: the 2011 Simav (Mw 5.8), 2017 Lesvos (Mw 6.3), and 2017 Bodrum-Kos (Mw 6.6) earthquakes. Source characteristics for these events are revealed using the EGF method across a broadband frequency range. SMGAs are defined as homogeneous rectangular fault planes characterized by large slip velocities and capable of reproducing strong ground motions [42]. The best source models are selected based on minimizing the average absolute residuals between observed and simulated pseudo-spectral accelerations (PSA). The study's findings, such as SMGAs and RTs, are compatible with global source-scaling relationships, as outlined by Somerville et al. [43]. Another important outcome is that the stress drop ratios, C, between mainshocks and aftershocks in normal-faulting earthquakes are markedly larger compared to previously calculated C values for strike-slip events in Turkiye. Finally, $\Delta\sigma$s within SMGAs are observed to be higher than the values calculated for the entire fault area; this finding was consistent with previous studies.

2. DATA USED IN THIS STUDY

In terms of large-magnitude earthquakes, the EAFZ maintained its seismic silence for many years. Furthermore, the quality and quantity of strong motion data from previous earthquakes were limited to perform comprehensive simulations. Hence, studies on the EAFZ have been relatively limited. At the beginning of this thesis in October 2022, except for the 2020 Mw 6.8 Sivrice Earthquake, the maximum magnitude of the events on EAFZ segments in the last 22 years was only 6.3 (Ms). The 2020 Mw 6.8 Sivrice earthquake on the Puturge segment of the EAFZ is a significant seismic event with accurate and reliable records. This earthquake released a substantial amount of seismic energy, similar to the 1905 earthquake (Ms 6.8) [34] (see Figure 1.3). Additionally, the availability of well-recorded moderate-sized aftershocks following the mainshocks enables the calculation of source parameters within the Puturge segment. The slip model of the event shows that the 2020 Sivrice (Mw 6.8) earthquake ruptured 45 km of the Puturge segment of the geologically determined 95 km long EAF [36]. This indicates that while accumulated stress remains in the unruptured sections of the Puturge segment fault line, the ongoing stress accumulation in adjacent segments continues to pose a significant hazard to the EAFZ. With the Mw 7.7 Nurdagi - Pazarcik earthquake that occurred on February 6, 2023, the Erkenek, Pazarcik, and Amanos segments located in the Main Strand ruptured; with Mw 7.6 Ekinozu - Elbistan earthquake, the entire Northern Strand ruptured. After these large earthquakes, two earthquakes with magnitudes larger than Mw 6.0 and numerous smaller magnitude aftershocks occurred. The existence of high-quality and processable earthquakes records have enabled the investigation of earthquake source parameters in these segments.

In this thesis, 11 medium-sized earthquakes with magnitudes of Mw 5.0 - 6.8 that occurred on the EAFZ are investigated. 11 aftershocks with magnitudes of Mw 4.0 - 5.0 were used as Green's function to find the source parameters of these earthquakes. A total of 86 strong motion stations are used to record earthquake data, with at least four strong motion stations per earthquake. The distribution of earthquake couples and strong motion stations is shown in Figure 2.1. The 11 earthquake pairs and horizontal component recording of 86 strong motion stations were selected according to the selection criteria explained in the following subchapter.

2.1. Selection Criteria

2.1.1. Station Selection Criteria

The selection of stations recording strong ground motions is very important. While the station set and number are selected differently when performing fc estimation analysis, the station set and number are selected differently when applying the EGF method. The general aim is to reach well-recorded earthquake records at the desired distance.

2.1.1.1. Station Selection for Corner Frequency (f_c) Estimation.

To determine the fc values of earthquakes, specific criteria are applied when selecting strong motion stations that record strong ground motions. Stations within a 100 km radius of the epicenter are prioritized, as beyond this distance, seismic waves become increasingly complex due to phenomena such as reflection and refraction. To minimize the influence of local site conditions, stiff-to-rock site stations are generally preferred. However, the majority of the strong motion stations in Turkiye are deployed either on soil and stiff sites. Hence, within this study, ground motion stations with a V_s30 value of 400 m/s or greater are preferred, reducing the potential impact of site effects on earthquake records.

The spatial distribution of selected stations is also carefully considered, ensuring the inclusion of at least one station in four different directions around the epicenter. Lastly, if an adequate number of suitable stations cannot be found within the 100 km radius, or if existing station records exhibit issues such as discontinuities, high noise levels, or other usability limitations, stations located within a radius of up to 150 km are incorporated into the analysis. f_c estimation does not require ground motion stations to record both the mainshock and aftershock simultaneously. Consequently, waveforms from 86 strong-motion stations meeting the necessary conditions within the defined boundaries were utilized. Comprehensive station information for each earthquake pair is detailed in Table 2.1.

2.1.1.2. Station Selection for EGF Method.

The selection of stations is a critical and challenging process, as only common ground motion stations that recorded both the mainshock and aftershock can be used in the analysis. Due to the limited number of stations, generally, all stations within a radius of 150 km from the epicenter of the earthquake are evaluated. The data from the stations recording the earthquake are first scanned and analyzed. If no discontinuity, distortion, or high level of noise is detected in the ground motion station records, these stations are directly included in the study.

One of the main advantages of the EGF approach is that while simulating a large earthquake, path and site effects are naturally present in small earthquake records and therefore, directly included in the simulation results. Consequently, the site effects for each earthquake remain within the waveform, so selecting stations does not necessarily require adherence to specific V_s30 thresholds. However, to ensure that earthquake couple records reflect similar path effects, the distance of the closest stations from the earthquake pair is generally limited to 10 times the distance between the mainshock and the aftershock. Exceptions to this rule may be made if no suitable station exists in the region and the closest station records produce accurate EGF results.

Additionally, the spatial distribution of the stations should be planned carefully. At least one station should be positioned in each of four directions (e.g., north, south, east, and west) around the earthquake epicenters. This distribution is crucial for minimizing the effects of rupture directivity and obtaining more balanced waveform data.

Unlike f_c estimation, recording data for both mainshocks and aftershocks is essential. To achieve this, 54 strong motion stations were employed, with a minimum of four stations per earthquake. Detailed descriptions of these earthquakes are provided in Figure 2.3 to Figure 2.16.

Table 2.1. The detailed information of the stations used in the EGF simulations and the fc estimations, are listed.

Station	Lat (°)	Long (°)	Vs30 (m/s)
0118	37.0362	35.3184	946
0119	36.5680	35.3900	485
0120	36.7701	35.7901	439
0122	37.4339	35.8202	501
0125	37.0152	35.7958	208
0127	37.8162	35.9204	583
0128	37.2503	35.0628	494
0129	38.2592	36.2109	965
0130	37.2519	35.6710	*
0201	37.7612	38.2674	391
0204	38.0290	39.0347	555
0205	37.7918	38.6160	660
0207	38.0323	38.2476	660
0212	38.0277	38.6241	*
0213	37.7967	37.9296	*
2104	38.2644	39.7590	*
2105	38.3581	40.0713	*
2107	38.1459	39.4838	*
2301	38.6704	39.1927	407
2302	38.3923	39.6754	907
2304	38.7210	39.8629	489
2305	38.7278	40.1310	907
2307	38.6958	39.9320	329
2308	38.4506	39.3102	450
2309	38.7991	38.7273	860
2310	38.5727	38.8245	*
2408	39.6019	39.0345	416
2409	39.2808	38.4911	875
2415	39.4610	38.5549	444
2703	37.0580	37.3500	758
2704	37.0088	37.8022	721
2705	37.0118	36.6206	720
2710	37.4329	37.6866	*
2711	37.3174	37.5604	*
2712	37.1840	36.7328	*
2713	37.4925	37.6241	*
2714	37.4922	37.6214	*
2718	37.0078	36.6266	*
3115	36.5463	36.1646	424
3116	36.6162	36.2066	870
3134	36.8276	36.2049	374
3135	36.4089	35.8831	460
3138	36.8026	36.5112	618
3142	36.4980	36.3661	539
3146	36.4908	36.2270	*
3147	35.9024	36.0644	*
3303	37.1659	34.6004	612
3304	36.3823	33.9366	297
3305	36.9214	34.8990	362
3802	38.4781	36.5036	305
3804	38.7227	36.3779	637
3805	38.1057	35.3572	384
4401	38.3496	38.3402	481
4404	38.1959	38.8739	1380
4405	38.8107	37.9396	579
4406	38.3439	37.9738	815
4407	38.7807	38.2641	735
4408	38.0962	37.8873	654
4409	38.5606	37.4908	*
4410	38.8668	37.6790	*
4411	39.0493	38.5034	*
4412	38.5969	38.1839	*
4413	38.3135	39.0393	*
4414	38.4069	38.7541	*
4611	37.7472	37.2843	731
4613	37.5701	36.3574	998
4614	37.4851	37.2978	671
4615	37.3868	37.1380	484
4617	37.5855	36.8303	574
4618	37.6001	36.8723	715
4619	37.5870	36.8662	545
4621	37.5935	36.9291	714
4623	37.5692	36.9340	561
4624	37.5361	36.9177	280
4625	37.5387	36.9819	346
4631	37.9663	37.4277	543
5807	38.7269	37.2475	445
6201	39.0747	39.5347	*
6302	37.2342	39.7509	1247
6303	37.7524	39.3291	986
6304	37.3651	38.5132	376
7901	36.7088	37.1123	463
8002	37.1916	36.5620	430
8003	37.0842	36.2694	350
8004	37.3799	36.0976	426
99007	35.5251	34.1750	575

2.1.2. Earthquake Selection Criteria

Given the limited number of earthquakes with moment magnitudes of 6.0 or greater along the EAFZ, the pool of eligible mainshock events is relatively small. Consequently, mainshocks were selected from earthquakes occurring either directly along the EAFZ or in close proximity to it. In this study, the magnitudes of the mainshock events range from Mw 5.0 to Mw 6.8.

To identify suitable aftershocks, a circle with a maximum radius of 6–7 km is drawn around the epicenter of the selected mainshock, and the presence of aftershocks within this area is evaluated. Seismic waveforms recorded at stations located beyond ten times the distance between the mainshock and aftershock epicenters ensure that seismic waves from both events are captured under similar path conditions. Strong motion stations at greater distances (>150 km) are restricted in the study. Therefore, as the distance between the mainshock and aftershock decreases, the number of strong motion stations available for analysis can increase. Moreover, at distances exceeding a certain threshold, waveforms recorded at strong motion stations may become more complex due to the arrival of refracted and reflected waves. These complexities can make the interpretation and analysis of waveform records more challenging. As illustrated in Figure 2.2, the aftershock with the Mw 5.1 on January 25, 2020, is located approximately 5–6 km away from the Mw 4.4 aftershock that occurred on the same day. If no aftershock is found within a 6-7 km distance, the mainshock is not considered suitable for EGF studies.

The fault mechanism solutions of aftershocks within the 6–7 km coverage area must closely match those of the mainshock. If there are significant differences in the focal mechanism solutions, depths, or other parameters of the earthquake couple, the aftershock is excluded from the analysis. On the other hand, fault mechanism solutions for small or some medium-sized earthquakes can not always be provided by earthquake monitoring institutes. In such cases, if there is no other aftershock to be used, the small-event focal mechanism solutions can be assumed to be the same as those for the mainshock. However, if the application of the EGF method yields poor results for this earthquake couple, it is removed from the study.

parameters. These divergences are clearly reflected in from Table 2.2 to Table 2.13. The reported values are carefully reviewed, and one of the results that are closely aligned with each other is selected.

Finally, when selecting earthquake couples with similar focal mechanisms and depth characteristics within the defined coverage area, the magnitude difference between the mainshock and the aftershock must not exceed 2 units. For instance, as illustrated in Figure 2.2, if the mainshock magnitude is 5.1, the aftershock magnitude is restricted to a maximum of 3.1. The characteristics of large earthquakes differ substantially from those of smaller ones. Large earthquakes typically occur along broader and deeper fault zones, while smaller earthquakes are confined to more localized areas and often exhibit simpler faulting mechanisms. Furthermore, a one-unit increase on the Richter magnitude scale (ML) corresponds to an approximately 32-fold increase in energy release. As a result, accurately capturing the complex dynamics of large earthquakes using data from much smaller events presents significant challenges. For this reason, Earthquake pairs with a magnitude difference of 2 or more are excluded from simulation analyses.

2.2. Earthquake Couples

2.2.1. 24 January 2020 Mw 6.8 (1m) Sivrice and 19 March 2020 Mw 5.0 (1a) Malatya Earthquakes

On January 24, 2020, at 17:55:11, a significant earthquake struck the Puturge segment of the EAFZ. According to reports from the United States Geological Survey (USGS), the earthquake reached an estimated intensity of IX on the Mercalli Intensity Scale. Shortly thereafter, on March 19, 2020, at 17:53:51, an aftershock occurred in close proximity along the same fault line. The characteristics of these seismic events, as reported by various institutes, earthquake observatories, and scholarly studies, are detailed in Table 2.2.

Table 2.2. Characteristics of the Mw 6.8 Sivrice Earthquake on January 24, 2020 and the Mw 5.0 Malatya Earthquake on March 19, 2020.

Lat (°)	Long (°)	Depth (km)	Magnitude (Mw)	Strike (°)	Dip (°)	Rake (°)	Strike (°)	Dip (°)	Rake (°)	Mo values	Source
For Mainshock											
38.3970	39.1730	9.40	6.8	248	76	1	*	*	*	*	[36]
38.4200	39.1400	15.80	6.8	247	72	-4	339	86	-162	1.96 E+19	MED_RCMT
38.5200	39.2900	10.00	6.7	339	85	-176	248	87	-4	1.29 E+19	KOERI
38.3593	39.0630	8.06	6.8	248	76	1	158	89	166	*	AFAD
38.2900	39.0200	12.00	6.8	245	67	-10	340	80	-156	1.76 E+19	GCMT
For Aftershock											
38.3720	39.1040	7.40	5.0	75	75	-19	*	*	*	*	[36]
38.3915	39.0729	10.00	*	65	64	10	330	81	153	4.73E+16	NEIC
38.4000	39.2200	18.10	5.2	68	78	5	337	85	168	6.81E+16	MED_RCMT
38.3500	39.0600	12.00	5.2	246	82	-25	340	65	-171	6.85E+16	GCMT
38.4000	39.0900	10.00	5.1	332	66	162	70	73	25	5.01E+16	KOERI
38.3720	39.1041	7.39	5.0	165	84	172	75	82	-6	*	AFAD

On the other hand, to achieve a more precise characterization of the seismic activity along the Puturge segment, Konca et al. [36] utilized a repositioned seismic activity catalog. Consequently, the earthquake parameters for both the mainshock and the aftershock were directly taken from the study conducted by Konca et al. [36]. Figure 2.3 depicts the locations of the 1st earthquake couple and the spatial distribution of stations that recorded both events.

Within the 100-150 km radius of the earthquake, no stations that met the required qualifications were identified in the southern or southeastern regions.

were no other earthquakes along the Puturge segment compatible with the mainshock for use in the EGF method, the records of the 2020 Mw 4.4 Sivrice earthquake were processed and utilized for analysis.

Multiple shock events are a common issue that arises when the time interval between two earthquakes is very short. This phenomenon occurs when one earthquake follows another in quick succession or when two earthquakes occur almost simultaneously. For example, in the E-W component recorded by station 4404 during the 2020 Mw 4.4 Sivrice earthquake, the accelerograph captured the acceleration values of three distinct seismic events within a single earthquake record (see Figure 2.5).

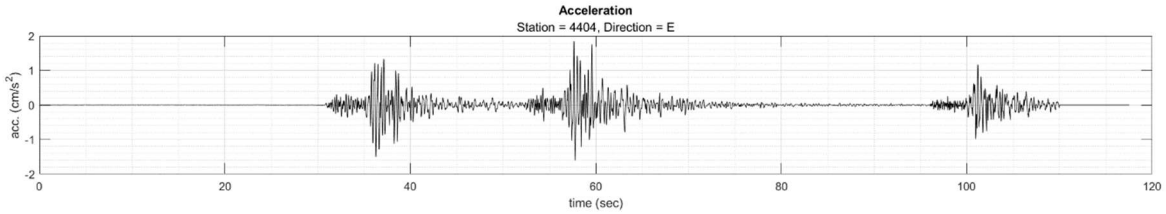


Figure 2.5. Acceleration time history of the 2020 Mw 4.4 Sivrice aftershock that occurred on January 25, 2020, recorded at station 4404.

The earthquake catalog published by KOERI was reviewed to examine all seismic records within the Puturge segment and its vicinity on the date and time of the small earthquake. According to the KOERI catalog, three earthquakes occurred in succession, which is consistent with the earthquake record provided by AFAD.

Table 2.4. Earthquakes that occurred around 16:40 on January 25, 2020, in the Puturge segment from KOERI earthquake catalog.

Earthquake ID	Date	Time	Lat (°)	Long (°)	Depth	Ml	Mw	Location
20200125164657	2020.01.25	16:46:57.79	38.4195	39.1263	5.0	4.1	4.0	ELAZIG
20200125164504	2020.01.25	16:45:04.62	38.4085	39.0400	13.7	3.5	*	ELAZIG
20200125164400	2020.01.25	16:44:00.80	38.4290	39.1558	5.0	3.8	*	ELAZIG

As reported by AFAD, the 2020 Mw 4.4 Sivrice aftershock occurred at 16:44:01. Similarly, KOERI data in Table 2.4 confirms that an earthquake took place at the same time. Following this event, two additional earthquakes were recorded in the same region on the same date, occurring at 16:45:04 and 16:46:57. Consequently, only the first earthquake record was processed, and the subsequent two records were excluded from the acceleration data.

2.2.3. 04 August 2020 Mw 5.6 (3m) Malatya and 04 August 2020 4.7 (3a) Malatya Earthquakes

Both earthquake couples analyzed in this study are aftershocks of the Mw 6.8 Sivrice earthquake that occurred on January 24, 2020. The Mw 5.6 Malatya earthquake, which took place on August 4, 2020, near the Yarpuzlu RSDB at the southern end of the Puturge segment, occurred at 09:37:34. Later that day, an Mw 4.7 aftershock was recorded at 18:40:03 in close proximity to the mainshock. Table 2.5 summarizes the characteristics of these seismic events as documented by various institutes and earthquake observatories.

Table 2.5. Characteristics of the Mw 5.6 Malatya Earthquake and the Mw 4.7 Malatya Earthquake on August 04, 2020.

Lat (º)	Long (º)	Depth (km)	Magnitude (Mw)	Strike (º)	Dip (º)	Rake (º)	Strike (º)	Dip (º)	Rake (º)	Mo values	Source
For Mainshock											
38.2193	38.7243	8.16	5.2	60	79	6	329	84	169	*	AFAD
38.1500	38.7200	12.90	5.6	235	75	-15	329	76	-165	2.74E+17	GCMT
38.1900	38.7200	13.40	5.6	56	88	18	325	72	178	2.89E+17	MED_RCMT
38.2000	38.6800	10.00	5.5	328	89	170	58	80	0	2.33E+17	KOERI
For Aftershock											
38.2386	38.7626	3.90	4.8	329	80	174	60	84	10	*	AFAD
38.2400	38.7600	15.30	4.7	62	87	42	329	48	175	1.23E+16	MED_RCMT
38.2374	38.7315	2.40	*	57	38	13	322	78	158	7.98E+15	NEIC
38.2168	38.7588	5.00	4.7	*	*	*	*	*	*	*	KOERI

whether the same result could be reproduced. The parameters and characteristics of the 4th earthquake couple are presented in Table 2.6.

Table 2.6. Characteristics of the Mw 5.6 Malatya Earthquake on August 04, 2020 and the Mw 4.4 Malatya Earthquake on February 11, 2023.

Lat (°)	Long (°)	Depth (km)	Magnitude (Mw)	Strike (°)	Dip (°)	Rake (°)	Strike (°)	Dip (°)	Rake (°)	Mo values	Source
For Mainshock											
38.2193	38.7243	8.16	5.2	60	79	6	329	84	169	*	AFAD
38.1500	38.7200	12.90	5.6	235	75	-15	329	76	-165	2.74E+17	GCMT
38.1900	38.7200	13.40	5.6	56	88	18	325	72	178	2.89E+17	MED_RCMT
38.2000	38.6800	10.00	5.5	328	89	170	58	80	0	2.33E+17	KOERI
*	*	*	*	*	*	*	*	*	*	2.82E+17	[63]
For Aftershock											
38.2080	38.7190	10.76	4.4	139	78	-178	48	88	-12	*	AFAD
38.1325	38.7320	3.00	*	*	*	*	*	*	*	*	NEIC
38.2150	38.7060	*	*	*	*	*	*	*	*	*	GFZ
38.1657	38.6955	5.00	4.4	*	*	*	*	*	*	*	KOERI
*	*	*	*	*	*	*	*	*	*	4.47E+15	[63]

Although the mainshock earthquake parameters have been announced by many institutions, there is limited information about the aftershock. However, the available data are sufficient to conduct earthquake simulations using these records of the two earthquakes and to investigate source properties. So, Figure 2.7 illustrates the locations of the selected earthquake pair, along with the stations that recorded them.

While the mainshock of the 3rd and 4th earthquake pairs is the same and the earthquake characteristics in both cases are taken from the values published by Med_RCMT, the aftershock characteristics of the 4th earthquake pair are taken from the values announced by KOERI. Additionally, no seismic moment value has been provided for the aftershock. Since the M_o is crucial for establishing scaling parameters in the EGF method, it is calculated theoretically using Equation (2.1) developed by Hanks and Kanamori [63]:

$$M_w = \frac{2}{3} log\, M_0 - 10.7 \tag{2.1}$$

2.2.6. 09 April 2022 Mw 5.2 (6m) Malatya and 09 April 2022 Mw 4.1 (6a) Malatya Earthquakes

It is an important earthquake pair that occurred on the Puturge segment. Both events took place on April 9, 2024, with the Mw 5.2 Malatya mainshock occurring at 14:02:14 and the Mw 4.1 Malatya aftershock occurring at 15:37:46. While focal mechanism solutions are available for the mainshock, no such data exists for the aftershock.

Table 2.8 presents the earthquake parameters and the values reported by various institutes for both events. The parameters provided by AFAD were selected for use in the EGF method to maintain consistency between the earthquake pairs.

Table 2.8. Characteristics of the Mw 5.2 Malatya Earthquake and the Mw 4.1 Malatya Earthquake on April 09, 2022.

Lat (º)	Long (º)	Depth (km)	Magnitude (Mw)	Strike (º)	Dip (º)	Rake (º)	Strike (º)	Dip (º)	Rake (º)	Mo values	Source
For Mainshock											
38.1550	38.6433	6.72	5.2	159	81	-165	67	75	-9	*	AFAD
38.1109	38.6642	6.00	5.3	242	87	-35	334	55	-177	7.26E+16	NEIC
38.1400	38.5700	14.00	5.3	248	83	-14	340	77	-173	1.05E+17	GCMT
38.1000	38.6300	10.00	5.2	339	71	-169	245	79	-18	7.30E+16	KOERI
*	*	*	*	*	*	*	*	*	*	7.08E+16	[63]
For Aftershock											
38.1706	38.6471	8.28	4.1	*	*	*	*	*	*	*	AFAD
38.1890	38.5615	13.60	3.8 (Ml)	*	*	*	*	*	*	*	KOERI
*	*	*	*	*	*	*	*	*	*	1.58E+15	[63]

As with some other earthquake couples, the M_o of the aftershock in this case is not provided. Therefore, M_o values were calculated theoretically for both the mainshock and the aftershock. Similarly, since no focal mechanism solution is available for the aftershock, it is assumed to have the same focal mechanism as the mainshock. Figure 2.10 illustrates the locations of the earthquake pair and the distribution of stations that recorded these events, based on the selected coordinates.

Table 2.9. Characteristics of the Mw 5.4 Adiyaman Earthquake and the Mw 4.0 Adiyaman Earthquake on February 07, 2023.

Lat (°)	Long (°)	Depth (km)	Magnitude (Mw)	Strike (°)	Dip (°)	Rake (°)	Strike (°)	Dip (°)	Rake (°)	Mo values	Source
For Mainshock											
37.8080	37.6550	8.44	5.4	224	83	-173	133	83	-7	*	AFAD
37.7900	37.6600	19.00	5.4	107	77	173	198	83	12	1.84E+17	KOERI
37.7700	37.7650	19.00	5.4	24	87	-26	115	64	-177	1.18E+17	GFZ
37.7586	37.7433	11.00	*	111	72	178	202	87	18	1.20E+17	NEIC
*	*	*	*	*	*	*	*	*	*	1.41E+17	[63]
For Aftershock											
37.7910	37.6770	9.71	4.4	115	25	159	225	81	67	*	AFAD
37.8233	37.5912	7.10	4.0	*	*	*	*	*	*	*	KOERI
37.7480	37.6323	*	*	*	*	*	*	*	*	*	NEIC
*	*	*	*	*	*	*	*	*	*	1.12E+15	[63]

The earthquake parameters for this earthquake couple were obtained from various institutes and observatories (see Table 2.9). However, as no institution provided M_o information for the small event, it was calculated theoretically. Figure 2.11 illustrates the coordinates of the mainshock and aftershock as well as the distributions of recording stations 2310, 2710, 4412, 4617, and 6304.

2.2.9. 20 February 2023 Mw 6.3 (9m) and 07 February 2023 Mw 4.8 (9a) Hatay Earthquakes

Following the Kahramanmaras earthquakes (Mw 7.7 and Mw 7.6) on February 6, 2023, thousands of aftershocks were recorded. However, only two aftershocks had magnitudes of 6.0 or greater. One of these was the 2023 Mw 6.3 Hatay earthquake, which occurred on February 20, 2023 at 17:04:27. This earthquake occurred in the Karasu REB, which includes Antakya and its surroundings.

The Karasu REB is morphologically and tectonically quite complex, and its intricacy is further heightened by the intersection of the Amanos segment of the EAFZ, the Antakya segment of the Cyprus Arc, and the Hacipasa segment of the Dead Sea Fault [23], [65]. Consequently, the Mw 6.3 Hatay earthquake holds significant importance for understanding the seismic source characteristics of the Antakya region.

Table 2.11. Characteristics of the Mw 6.3 Hatay Earthquake on February 20, 2023 and the Mw 4.8 Hatay Earthquake on February 07, 2023.

Lat (º)	Long (º)	Depth (km)	Magnitude (Mw)	Strike (º)	Dip (º)	Rake (º)	Strike (º)	Dip (º)	Rake (º)	Mo values	Source
For Mainshock											
36.0370	36.0210	21.73	6.4	214	57	-44	332	55	-138	*	AFAD
36.0600	36.0300	12.00	6.3	226	42	-16	328	79	-131	4.09E+18	GCMT
36.2269	36.0062	11.50	*	225	53	-27	333	69	-139	4.09E+18	NEIC
36.1240	35.9400	15.00	6.3	228	35	-17	332	81	-124	4.09E+18	GFZ
36.1000	36.1300	16.00	6.3	330	68	-143	225	56	-25	3.63E+18	KOERI
For Aftershock											
36.0710	35.9570	10.76	4.7	319	65	-150	216	63	-28	*	AFAD
35.9600	35.8500	16.50	4.8	219	57	-25	323	69	-145	2.40E+16	GCMT
35.9675	35.9849	11.00	*	124	86	146	217	56	5	1.27E+16	NEIC
35.9220	36.0167	2.50	*	*	*	*	*	*	*	*	KOERI

For earthquake simulations, the Mw 4.8 Hatay earthquake, which occurred on February 7, 2023, at 02:47:37, was selected as Green's function pair for the Mw 6.3 Hatay

provided in terms of body wave magnitude and Richter magnitude scale. These parameters are summarized in Table 2.12.

Table 2.12. Characteristics of the Mw 5.8 Osmaniye Earthquake on February 06, 2023 and the Mw 4.0 Gaziantep Earthquake on February 09, 2023.

Lat (º)	Long (º)	Depth (km)	Magnitude (Mw)	Strike (º)	Dip (º)	Rake (º)	Strike (º)	Dip (º)	Rake (º)	Mo values	Source
For Mainshock											
37.1280	36.6390	11.19	5.7 (Ml)	26	56	-121	254	45	-52	*	AFAD
36.9921	36.6832	10.00	5.6 (Mb)	*	*	*	*	*	*	*	NEIC
37.0485	36.4047	8.20	5.6 (Ml)	*	*	*	*	*	*	*	KOERI
*	*	*	*	*	*	*	*	*	*	5.62E+17	[63]
For Aftershock											
37.1360	36.6570	7.00	4.1 (Ml)	11	57	-110	225	38	-62	*	AFAD
37.1058	36.6317	5.50	4.2 (Mb)	*	*	*	*	*	*	*	NEIC
36.9750	36.6858	10.10	4.2 (Mw)	*	*	*	*	*	*	*	KOERI
*	*	*	*	*	*	*	*	*	*	4.47E+15	[63]

The body wave magnitudes reported by NEIC for the mainshock and aftershock were 5.6 and 4.2, respectively. Using Kadirioğlu's Equation (2.3) [64], these values were converted to moment magnitudes of 5.8 (ranging from 5.5 to 6.1) for the mainshock and 4.4 (ranging from 4.1 to 4.6) for the aftershock.

$$M_w = 1.0319\ (\pm 0.025)\ M_b + 0.0223\ (\pm 0.130) \quad (2.3)$$

The M_o values for the 2023 Mw 5.8 Osmaniye earthquake and the 2023 Mw 4.4 Gaziantep earthquake, which together form the 10th earthquake pair, were not reported. Consequently, the M_o values for both events were calculated using a theoretical formula (see Equation (2.1). Figure 2.14 illustrates the distribution of stations -0119, 0127, 0128, 0129, 2704, and 4615- that recorded the seismic waves from the mainshock and aftershock.

To simulate the Mw 5.0 earthquake, the Mw 4.0 Kahramanmaras earthquake, which occurred on August 26, 2015, at 23:01:44, was selected as the aftershock, as it is the closest event to the 2023 Mw 6.7 Gaziantep earthquake. The parameters of the 2015 Mw 4.0 Kahramanmaras earthquake were applied to both the simulated Mw 5.0 earthquake and the original Mw 4.0 event. The characteristics of the 2023 Mw 6.7 Gaziantep earthquake and the 2015 Mw 4.0 Kahramanmaras earthquake are detailed in Table 2.13.

Table 2.13. Characteristics of Mw 6.7 Gaziantep Earthquake on the February 06, 2023 and the Mw 4.0 Kahramanmaras Earthquake Augus 26, 2015.

Lat (º)	Long (º)	Depth (km)	Magnitude (Mw)	Strike (º)	Dip (º)	Rake (º)	Strike (º)	Dip (º)	Rake (º)	Mo values	Source
For Mainshock											
37.3040	36.9200	6.20	6.6	300	70	-128	187	43	-30	*	AFAD
37.2100	36.8400	26.20	6.8	306	78	-163	212	73	-13	1.86E+19	GCMT
37.1893	36.8929	9.80	6.7	*	*	*	*	*	*	*	NEIC
37.2127	36.7770	5.00	6.60 (Ml)	*	*	*	*	*	*	*	KOERI
37.2600	36.8500	16.30	6.7	306	52	178	37	88	38	*	MED_RCMT
*	*	*	*	*	*	*	*	*	*	1.26E+19	[63]
For Mw 5.0 Simulated Earthquake (Blind EGF Simulation)											
37.3000	36.9800	7.00	5.0	353	43	-100	187	48	-81	*	++
*	*	*	*	*	*	*	*	*	*	3.55E+16	[63]
For Aftershock											
37.3268	36.9318	9.23	4.0	*	*	*	*	*	*	*	AFAD
37.2895	36.9755	7.30	4.1 (Mb)	*	*	*	*	*	*	*	ISC
37.2743	36.9989	5.70	*	*	*	*	*	*	*	*	NEIC
37.3000	36.9800	7.00	4.0	353	43	-100	187	48	-81	9.72E+14	KOERI
*	*	*	*	*	*	*	*	*	*	1.12E+15	[63]

++: The earthquake parameters was taken as the same as the 2015 Mw 4.0 Kahramanmaraş aftershock.

The coordinates, depth, and focal mechanism solution of the artificially generated Mw 5.0 earthquake were assumed to be identical to those of the Mw 4.0 earthquake that occurred in 2015. However, although the M_o of the 2015 Mw 4.0 Kahramanmaras

Table 2.14. Earthquake locations and parameters.

Earthquake No	Lat (º)	Long (º)	Depth (km)	Magnitude (Mw)	Strike (º)	Dip (º)	Rake (º)	Mo values	Sources				
									Location	Depth	Magnitude	Focal Mechanism	Seismic Moment
1 m	38.3970	39.1730	9.40	6.80	248	76	1	1.29E+19	[36]	[36]	[36]	[36]	KOERI
1 a	38.3720	39.1040	7.40	5.00	75	75	-19	4.73E+16	[36]	[36]	[36]	[36]	NEIC
2 m	38.3170	39.1040	16.00	5.10	234	76	-13	6.46E+16	GFZ	GFZ	GCMT	NEIC	MED_RCMT
2 a	38.3926	39.1235	11.86	4.40	247	74	-13	7.80E+15	AFAD	AFAD	AFAD	AFAD	MED_RCMT
3 m	38.1900	38.7200	13.40	5.60	56	88	18	2.89E+17	MED_RCMT	MED_RCMT	MED_RCMT	MED_RCMT	MED_RCMT
3 a	38.2400	38.7600	15.30	4.70	62	87	42	1.23E+16	MED_RCMT	MED_RCMT	MED_RCMT	MED_RCMT	MED_RCMT
4 m	38.1900	38.7200	13.40	5.60	56	88	18	2.82E+17	MED_RCMT	MED_RCMT	MED_RCMT	MED_RCMT	[63]
4 a	38.1657	38.6955	5.00	4.40	48	88	-12	4.47E+15	KOERI	KOERI	KOERI	AFAD	[63]
5 m	38.4100	39.2000	11.50	5.60	231	36	-22	2.82E+17	GCMT	NEIC	GCMT	GCMT	[63]
5 a	38.4941	39.1935	17.14	4.30	231	36	-22	3.16E+15	AFAD	AFAD	AFAD	*	[63]
6 m	38.1550	38.6433	6.72	5.20	242	87	-35	7.08E+16	AFAD	AFAD	AFAD	NEIC	[63]
6 a	38.1706	38.6471	8.28	4.10	242	87	-35	1.58E+15	AFAD	AFAD	AFAD	*	[63]
7 m	37.7586	37.7433	11.00	5.40	202	87	18	1.41E+17	NEIC	NEIC	GFZ	NEIC	[63]
7 a	37.7480	37.6323	7.10	4.00	225	81	67	1.12E+15	NEIC	KOERI	KOERI	AFAD	[63]
8 m	37.4805	37.1180	5.80	5.30	317	40	-124	1.00E+17	KOERI	KOERI	AFAD	AFAD	[63]
8 a	37.4472	37.0528	5.60	4.00	270	75	-127	1.12E+15	KOERI	KOERI	AFAD	AFAD	[63]
9 m	36.0600	36.0300	12.00	6.30	226	42	-16	4.09E+18	GCMT	GCMT	GCMT	GCMT	GCMT
9 a	35.9600	35.8500	16.50	4.80	219	57	-25	2.40E+16	GCMT	GCMT	GCMT	GCMT	GCMT

10 m	37.0485	36.4047	8.20	5.80	26	56	-121	5.62E+17	KOERI	KOERI	NEIC	AFAD	[63]
10 a	36.9750	36.6858	10.10	4.40	11	57	-110	4.47E+15	KOERI	KOERI	NEIC	AFAD	[63]
11 m	37.2100	36.8400	9.80	6.70	212	73	-13	1.26E+19	GCMT	NEIC	NEIC	GCMT	[63]
11 blind	37.3000	36.9800	7.00	5.00	187	48	-81	3.55E+16	Ψ	Ψ	Ψ	Ψ	
11 a	37.3000	36.9800	7.00	4.00	187	48	-81	1.12E+15	KOERI	KOERI	KOERI	KOERI	[63]

*: Focal mechanism solutions are unavailable and have been assumed to be identical to those of the mainshock. Ψ: It was assumed that the earthquake parameters are the same as those in 11a.

3. METHOD of ANALYSIS

3.1. Brune Spectrum

Among various earthquake source models, the classical model introduced by J. Brune in the early 1970s remains a cornerstone in seismology [3]. This model provides a foundational approach for analyzing fault rupture propagation and the radiation of seismic energy. At its core, the Brune source model assumes a circular fault geometry with a uniform $\Delta\sigma$, offering a simplified yet effective representation of earthquake rupture dynamics (e.g., [66-68]).

In this framework, the shear wave spectrum at an observation point located R kilometers from the seismic source can be described using the point source model introduced by Brune [3], [69], which incorporates a single fc. According to this model, the observed waveform A (t) can be expressed in the time domain:

$$A(t) = S(t) * P(t) * G(t) \tag{3.1}$$

Here,

The observed waveform A (t) represents the convolution of three primary effects, assuming the system exhibits linear behavior:

- Source effect S (t): Captures the influence of the rupture process occurring on the fault surface.
- Propagation path effect P (t): Explains the transmission of seismic waves from the source to the site.
- Site amplification effect G (t): Reflects the impact of sedimentary layers on seismic waves as they propagate to the surface.

In the frequency domain, the observed spectrum A (f) can be described as the product of these effects:

$$A(f) = S(f) \,.\, P(f) \,.\, G(f) \tag{3.2}$$

acceleration source spectrum increases proportionally to the square of the frequency at frequencies below f_c and remains constant at frequencies above f_c. This behavior is illustrated in Figure 3.1. The source effects are represented mathematically like:

$$S(f) = C \,.\, Mo \,.\, S(f, fc) \tag{3.3}$$

where, M_o represents the seismic moment, measured in Newton-meters (N.m), quantifying the earthquake's overall size. It can be easily calculated with Equation (2.1). The parameter f_c denotes the corner frequency, measured in Hertz (Hz), while S (f, fc) corresponds to the source spectrum. The scaling constant C comprises several fixed values, including the average radiation pattern ($R_{\theta\phi}$) for the S wave, the free surface amplification factor (FS), the average crustal density (ρ), the average Shear wave velocity (V_s), the coefficient representing partition of S wave energy into two horizontal components (PRTITN). In this case, the value of C is:

$$C = \frac{R\theta \quad FS \;\; PRTITN}{4 \;\pi\; \rho \;\; Vs^3} \tag{3.4}$$

Lastly, ın the ω^{-2} model, the acceleration Fourier amplitude spectrum (FAS), acceleration source spectrum, of the seismic wave radiating from the source is expressed by the following equation:

$$S(f, fc) = \frac{(2\,\pi\, f)^2}{1+\left(\frac{f}{fc}\right)^2} \tag{3.5}$$

The general form of the source effects can be rewritten as follows:

$$S(f) = \frac{R\theta\phi \;\; FS \;\; PRTITN}{4 \;\pi\; \rho \;\; Vs^3} \;\; Mo \;\; \frac{(2\,\pi\, f)^2}{1+\left(\frac{f}{fc}\right)^2} \tag{3.6}$$

3.1.2. Path Effects, *P (f)*

Path effects significantly influence the characteristics of GM records by altering the frequency content, amplitude, and velocity of seismic waves as they propagate through the Earth. Fundamentally, path effects describe the reduction in wave energy as seismic waves traverse the Earth's subsurface. This energy loss of seismic waves during propagation is explained by two primary mechanisms: elastic attenuation and anelastic attenuation.

- Geometric Spreading (Elastic Attenuation)

Also known as elastic attenuation, this phenomenon occurs as seismic wave energy diminishes with increasing distance from the source. The reduction in energy results from the geometric spreading of wavefronts as they radiate outward from the source.

- Anelastic Attenuation

  This mechanism involves wave energy dissipation into heat as seismic waves propagate through the Earth's materials. Anelastic attenuation is commonly modeled using the quality factor (Q (f)), which quantifies the Earth's efficiency in transmitting seismic waves without substantial energy loss. A higher Q (f) value indicates less inelastic damping along the wave's propagation path.

The combined effects of geometric spreading and anelastic attenuation are mathematically described by the path effect Equation (3.7). This formula effectively incorporates both mechanisms to describe how seismic waves lose energy as they travel through the Earth's subsurface. The path effects are modeled as follows:

$$P(f) = G(R)\, \mathrm{e}^{-\frac{\pi f R}{Q(f)Vs}} \tag{3.7}$$

where, R, G (R), and Q (f) represent the source-to-site distance, the geometrical spreading function, and the frequency-dependent quality factor, respectively.

In Equation (3.8), G (R) represents geometric spreading, a mathematical function that characterizes how the amplitude of seismic waves varies with distance from the earthquake source. Boore [72] described G (R) as a piecewise continuous function, as it is composed of distinct segments or regions, each corresponding to specific distance intervals from the source.

$$G(R) = \begin{cases} \frac{R0}{R}, & R \le R1 \\ G(R1)\left(\frac{R1}{R}\right)p1, & R1 \le R \le R2 \\ G(Rn)\left(\frac{Rn}{R}\right)pn, & R \ge Rn \end{cases} \tag{3.8}$$

In Equation (3.7), G (R) represents elastic attenuation, while the exponential term accounts for anelastic attenuation. This anelastic attenuation, which describes the energy loss of seismic waves as they propagate through the Earth's medium, is quantified using the Q (f) [73].

The value of Q (f) varies significantly across different regions of the world, reflecting differences in seismotectonic characteristics [74, 75]. Therefore, selecting an appropriate Q

value that corresponds to the specific seismic region under investigation is essential for accurate modeling. The quality factor Q (f) is generally expressed as:

$$Q(f) = Qo\, f^{n} \tag{3.9}$$

where, the constant Q_o represents the heterogeneous behavior of the medium, while the parameter n is directly proportional to the region's seismicity [76]. Generally, the Q-value exhibits frequency independence for frequencies below 1 Hz, whereas it becomes frequency-dependent for frequencies greater than 1 Hz, increasing with rising frequency [75]. Accurately estimating the Q (f) is crucial for obtaining realistic high-frequency ground motion spectra, as it directly influences the attenuation characteristics of seismic waves [77].

3.1.3. Site Effects, *G (f)*

Sediments located near the ground surface, comprising the uppermost several hundred meters of soil and rock, play a crucial role in influencing the amplitude, frequency characteristics, and duration of seismic waves. This phenomenon, known as the site effect, is a key factor in assessing seismic hazards and devising mitigation strategies.

Site effects generally amplify seismic waves due to the impedance contrast between softer surface materials, such as sediments, and the denser, more rigid underlying bedrock. Conversely, local soils may also attenuate certain frequencies through material damping, a process where seismic energy is dissipated as heat.

To quantify the amplification and attenuation of seismic waves caused by site effects, a site response function, G (f), is commonly used. This function is expressed as:

$$G(f) = AA(f)\, D(f) \tag{3.10}$$

Here, AA (f) represents the amplification of seismic waves due to impedance contrasts between subsurface layers. In contrast, D (f) refers to the diminution factor, which reflects the energy loss caused by material damping.

3.1.3.1. Amplification Factors, *AA (f)*.

The difference in seismic impedance between two soil layers, defined as the resistance of a medium to particle motion, significantly changes the amplitude of seismic waves. Typically, soil density and wave velocity decrease progressively from bedrock toward the ground surface. As seismic waves propagate from the source to the surface, this reduction in impedance causes the particle velocity and, consequently, the wave amplitudes to increase in order to conserve elastic wave energy. This phenomenon is referred to as site amplification.

To accurately understand site effects, it is essential to determine the soil properties and evaluate site amplification. Site amplification models can be developed depending on whether the velocity profile of the local soil layers is known.

When the wave velocity profile of a region is known, amplification factors can be determined using theoretical transfer functions. These are typically calculated using 1D models [78], 2D models [79], or 3D models [80] of the soil medium.

Alternatively, Boore and Joyner [81] introduced the quarter-wavelength approximation method to estimate site responses. In this approach, amplification at a specific frequency is determined by considering the ratio of the seismic impedance at the source level to the average seismic impedance at a given depth. This relationship can be expressed as:

$$AA(f) = \sqrt{\frac{\rho s\, Vs}{\rho(z)\, Vs(z)}} \tag{3.11}$$

where, ρs and ρ(z) represent the density at the source and the travel-time-weighted average density, respectively, Vs and Vs(z) and denote the S-wave velocity at the source and the average S-wave velocity to depth z.

3.1.3.2. Diminution Factors, *D (f)*.

The diminution function for site effects refers to the attenuation or reduction of seismic wave energy as it propagates local geological materials. Although site effects often amplify GM due to impedance contrasts or resonance in softer soils, specific conditions can result in energy dissipation or reduction. This diminution function, influenced by various physical and material properties of the site, quantifies the extent of this attenuation.

This decay mechanism is distinct from the attenuation caused by wave propagation along the seismic path [8]. The exact cause of high-frequency decay remains a topic of discussion, with some attributing it to source properties and others to site effects. Two primary approaches are widely used to model this decay: the f-max approach and the kappa (κ) parameter.

Hanks [82] attributes this phenomenon to attenuation in near-surface soil layers. Proposed by Hanks [82], the f-max approach introduces a cut-off frequency for the seismogram, beyond which high-frequency components are significantly attenuated. The mathematical expression of this concept can be articulated as follows:

$$D(f) = \left[1 + \left(\frac{f}{fmax} \right)^8 \right]^{-1/2} \tag{3.12}$$

On the other hand, Papageorgiou and Aki [83] propose that the reduction in high-frequencies is associated with the processes occurring at the earthquake source. The κ parameter, introduced by Anderson and Hough [84], provides an alternative method for modeling high-frequency spectral attenuation in seismic ground motion records. This approach characterizes the attenuation of high-frequency GM using an exponential decay function.

$$D(f) = e^{-\pi \, \mathrm{Ko} \, f} \tag{3.13}$$

where, the parameter κ_o represents near-surface attenuation due to the distance from the earthquake source to the site.

The observed amplitude spectrum is initially and typically expressed as Equation (3.2). When the source, path, and site effects are explicitly included in terms of acceleration, the equation can be written as:

$$A(f) = C \; Mo \; \frac{(2\,\pi\, f)^2}{1+\left(\frac{f}{fc}\right)^2} \; G(R) \; \mathrm{e}^{-\frac{\pi f R}{Q(f) Vs}} \; e^{-\pi \, \mathrm{Ko} \, f} \; G(f) \tag{3.14}$$

When estimating the f_c, the source spectrum is obtained by dividing the shear wave acceleration spectrum A(f), recorded at an observation point located R kilometers from the source, by the path and site effects, following Brune's model [3], [69]. At the onset of this study, specific values for the quality factor Q (f) and attenuation parameter κ for the EAFZ and its fault segments were not available. As a result, both exponential attenuation terms were neglected. Similarly, strong ground motion stations located on soil with V_s30 values

greater than 400 m/s were selected to minimize the influence of site amplification. This allowed the site amplification term G (f) to be neglected as well.

Geometrical spreading at local and regional distances depends on wave phase, distance, depth, and regional characteristics. Although Boore [72] provides detailed guidelines for geometrical spreading, this study adopted the widely accepted relationship for direct waves at short distances, where the amplitude decreases proportionally to 1/R [85]. Therefore, the shear wave acceleration spectrum A (f), recorded at a distance R from the source, was adjusted using the geometrical spreading factor and used to determine the source spectrum at the earthquake source. For the earthquakes analyzed in this study, generally occurring within 150 km of recording stations, attenuation due to geometric spreading was assumed to follow G(R) = 1/R for S-waves.

3.2. Strong Ground Motion Simulation

The availability of strong ground motion records has greatly advanced our understanding of earthquake rupture processes, propagation path effects, site amplification/diminution effects, and the relationship between GM and resultant damage. However, it becomes difficult to perform detailed analyses in some geographical regions where seismic data are sparse or strong ground motion records are unavailable.

In such cases, simulated earthquake motions provide a valuable alternative for estimating earthquake parameters, characterizing source mechanisms, evaluating propagation path effects, assessing site amplification, and understanding their relationship with GM and damage. Moreover, the ability to predict strong ground motions using various simulation methods plays a critical role in mitigating the impact of future earthquakes and improving disaster preparedness and resilience.

Earthquake GM can be simulated using three primary approaches, each suited to different frequency ranges and modeling needs. The stochastic simulation method is particularly effective for high-frequency GM modeling, capturing the random variability of seismic wave behavior. On the other hand, the deterministic simulation approach is most applicable for modeling low-frequency GM, where physical processes can be represented in

detail. Both methods provide critical knowledge of the frequency-dependent mechanisms governing strong ground motion.

The hybrid simulation method combines the strengths of stochastic and deterministic simulations. By leveraging both advantages, the hybrid method offers a comprehensive illustration for modeling GM across a broader frequency spectrum.

Stochastic methods:

Hanks and McGuire [86] combined seismological models for the spectral amplitude of GM with the approach that high-frequency motions are inherently random. It is well-established that high-frequency accelerations exhibit irregularity due to various factors. These inconsistencies are challenging to predict/model deterministically, making stochastic models an essential tool for simulating strong ground motion.

The stochastic approach addresses these irregularities by utilizing random processes to replicate the statistical characteristics of observed GMs rather than detailing the physical modeling of seismic wave propagation. That is, for high-frequency GMs, Green's functions are calculated through a stochastic methodology that employs random summation.

Stochastic methods are particularly effective in simulating GMs at 1-2 Hz to 20 Hz or higher frequencies. The lower limit of 1 Hz is typically chosen to avoid overlap with deterministic models, which provide greater accuracy at lower frequencies.

Deterministic methods:

Deterministic GM simulations utilize a physics-based approach to predict earthquake GMs by explicitly modeling the source, propagation path, and site effects of seismic waves in accordance with deterministic physical principles. That is, for low-frequency GMs, Green's functions are calculated using deterministic methods that employ coherent summation of rays or wave-numbers.

Various methodologies have been developed to achieve deterministic simulations of strong ground motions, such as the discrete wave-number, modal summation, ray theory, 2.5-D pseudo-spectral, and 2.5-D finite difference methods.

Small-scale heterogeneities significantly influence high-frequency waveforms exceeding 2 Hz. Therefore, Deterministic methods are generally valid for simulating GMs within the frequency range of 0.01 Hz to 1–2 Hz.

Hybrid methods:

Deterministic methods offer detailed physical modeling of seismic wave propagation at low frequencies, while stochastic methods capture the complexity of high-frequency GMs. However, neither approach alone is capable of accurately simulating GMs over a broad frequency range. Combining both methods' strengths, hybrid simulations offer a comprehensive and realistic representation of earthquake GM across an extended frequency spectrum. This integrated approach provides accurate and practical simulations over a wide frequency band by taking advantage of the precision of deterministic modeling for low frequencies and the efficiency of stochastic techniques for high frequencies.

It is known that Green's functions for low-frequency GMs are typically calculated using deterministic methods, whereas high-frequency GMs are often derived through stochastic approaches.

The EGF method can sometimes be combined with stochastic elements in hybrid simulations to extend its applicability to higher frequencies. Despite this flexibility, the core principles of the EGF method remain grounded in deterministic approaches. Unlike purely theoretical deterministic approaches, the EGF method utilizes observed GM records from smaller earthquakes (subevents) to simulate the GM of larger events. This is because aftershock records inherently account for propagation path effects and local site effects, making EGF a practical tool for estimating broadband motions. The frequency range of the EGF simulation is contingent on the quality and resolution of the observed subevent records. As long as the aftershock records are accurate over a broad frequency range, the EGF method provides reliable estimates of broadband ground motions.

Irikura [6], [9] first introduced the concept of simulating large seismic events using smaller events. The EGF-based source modeling technique, further developed by Irikura [9] and Kamae and Irikura [87], facilitates the characterization of near-source strong ground

motions within a broadband frequency range, typically extending up to 10 Hz. This method is widely regarded as one of the most efficient and accurate techniques for detecting SMGAs.

3.2.1. Empirical Green's Function (EGF) Method

Initially proposed by Hartzell [7], the EGF method offers a semi-empirical approach to synthesizing waveforms for large events using actual small-event records rather than relying on theoretical Green's functions.

Since Hartzell's work, the semi-empirical approach has been extensively developed by researchers such as Kanamori [88]; Irikura [6], [9]; Dan et al. [89]; Irikura and Kamae [90]; Kamae and Irikura [87]; and Miyake et al. [42]. Irikura's [9] formulation incorporates a scaling law for fault parameters between large and small events from Kanamori and Anderson [41], and the omega-squared source spectral model from Aki [71] and Brune [3], [69].

In this approach, the waveform of a large earthquake is synthesized by summing the records of small events while accounting for variations in their slip velocity time functions [87]. Importantly, explicit information about the slip velocity-time function of the small events is not necessary. Instead, the fault plane of the target event is divided into N×N subfaults, each corresponding in size to the rupture area of the small event. The GM contribution of each subfault is derived from the observed record of the small event, which serves as Green's function.

The frequency range over which this method is applicable depends on the signal-to-noise ratios of the GM records from the smaller events[48]. The numerical equations for summing records of small events are:

$$U(t) = \sum_{i=1}^{N} \sum_{j=1}^{N} \frac{r}{r_{ij}} F(t) * (C \,.\, u(t)) \tag{3.15}$$

$$F(t) = \delta\left(t - t_{ij}\right) + \frac{1}{n\prime\left(1-\frac{1}{e}\right)} \sum_{k=1}^{(N-1)\,n\prime} \left[\frac{1}{\frac{(k-1)}{e^{(N-1)\,n\prime}}} \delta\left\{t - tij - \frac{(k-1)T}{(N-1)\,n\prime}\right\}\right] \tag{3.16}$$

$$tij = \frac{r_{ij} - r_o}{V_s} + \frac{\xi_{ij}}{V_r} \tag{3.17}$$

where, U (t) represents the simulated waveform for the large event, while u (t) denotes the observed waveform for the small event. The scaling parameters N and C correspond to the ratios of the dimensions of the SMGA and the stress drops between the large and small events, respectively. The asterisk (*) indicates convolution. The filtering function, F (t), is used to adjust for differences in the slip velocity time functions of the large and small events. Irikura et al. [91] defined F (t) as an exponentially decaying function. T represents the RT of the large event, which is the duration of the filtering function F (t) (see Figure 3.2). An integer n′ is introduced to shift the artificial periodicity to a frequency range higher than the one of interest [87]. The distances r, r_{ij}, and r_o are defined as follows:

- r is the distance from the site to the hypocenter of the small event,
- r_{ij} is the distance from the site to the (i,j) sub-fault, and
- r_o is the distance from the site to the rupture starting point (RSP) on the large event's fault plane.

Additionally, ξ_{ij} represents the distance between the RSP and the (i, j) subfault. The parameters V_s and V_r refer to the S-wave velocity in the source area and the rupture velocity on the fault plane, respectively. The relationship between V_s and V_r is known to vary across different regions. For this study, the formulation proposed by Cheloni and Akinci [92] is adopted to define this relationship.

$$Vr = 0.8\,Vs \tag{3.18}$$

In Irikura [9], the scaling parameters required for this method, N and C, can be determined using the constant levels of the displacement and acceleration amplitude spectra of the large and small events. These parameters are calculated using the following formulas:

$$\frac{U_o}{u_o} = \frac{M_o}{m_o} = CN^3 \tag{3.19}$$

$$\frac{A_o}{a_o} = CN \tag{3.20}$$

Here,

- U_o and u_o represent the constant levels of the displacement amplitude spectra for the large and small events, respectively.
- M_o and m_o correspond to the seismic moments of large and small events.
- A_o and a_o denote the constant levels of the acceleration amplitude spectra for the large and small events.

Using Equation (3.22), the source spectral ratio function (SSRF) is:

$$SSRF(f) = \frac{Mo}{mo} \frac{1+\left(f/f_{ca}\right)^2}{1+\left(f/f_{cm}\right)^2} \tag{3.23}$$

M_o and m_o represent the seismic moments of the mainshock and aftershock, respectively. Similarly, f_{cm} and f_{ca} denote the corner frequencies of the mainshock and aftershock.

To estimate the parameters M_o, m_o, f_{cm}, and f_{ca}, the weighted least squares method (Equation (3.24)) was applied to the observed source amplitude spectral ratio (Equation (3.21)). This approach aimed to achieve the best possible fit to the Source Spectral Ratio Function (SSRF) (Equation (3.23)) within the frequency domain.

$$\sum_{i=1}^{m} \left(\frac{SSRF(fi) - S(fi)/s(fi)}{SD(fi)}\right)^2 = min \tag{3.24}$$

The relationships between the scaling parameters N and C are expressed as:

$$\frac{M_o}{m_o} = CN^3 \qquad (f \to 0) \tag{3.25}$$

$$\left(\frac{M_o}{m_o}\right)\left(\frac{f_{cm}}{f_{ca}}\right)^2 = CN \qquad (f \to \infty) \tag{3.26}$$

The high-frequency limit is defined as the frequency range where the acceleration source spectrum remains constant, specifically for frequencies greater than f_{ca} and less than f_{max}. Here, f_{max} represents the high-frequency cutoff of the constant level of the acceleration source spectrum. Based on Equation (3.25) and Equation (3.26), the parameters N and C are expressed as follows:

$$N = \left(\frac{f_{ca}}{f_{cm}}\right) \tag{3.27}$$

$$C = \left(\frac{Mo}{mo}\right)\left(\frac{f_{cm}}{f_{ca}}\right)^3 \tag{3.28}$$

3.3. Evaluating Goodness-Of-Fit (GOF) Of Waveform

Simulated GMs have gained significant attention in seismology and earthquake engineering due to their utility in estimating source parameters that are difficult to determine, such as the SMGA, RT, and RSP. However, the accuracy and reliability of these source

parameters critically depend on the success of the simulations, which, in turn, rely on the consistency between synthetic waveforms produced by the simulations and observed waveforms in both the time and frequency domains.

To evaluate simulation accuracy, researchers compare synthetic waveforms with observed mainshock data to identify the best-fit source model. This involves assessing the agreement between the synthetic and observed waveforms regarding key metrics such as acceleration, velocity, and displacement. Traditionally, many researchers have relied on single parameters like PGA, PGV, PGD, or spectral acceleration (SA) to evaluate the fit (e.g., [93]). Others have relied on visual inspections to determine the fit between observed and synthetic waveforms (e.g., [52]). While these approaches may yield satisfactory results for acceleration, velocity, and displacement at many stations, using a single parameter often fails to produce consistently accurate simulation outcomes.

Despite the availability of various methods to assess the fit between observed and synthetic waveforms, there is no consensus on which parameter best represents the goodness-of-fit (GOF). To address this challenge, a quantitative method is essential for systematically evaluating the fit [94-96]. The GOF methodology focuses on comparing specific features of synthetic and observed seismograms in both the time and frequency domains. Researchers typically define GOF criteria based on parameters selected for their specific study. Recently, studies have explored GOF criteria that assess the fit between observed and simulated seismic waveforms, incorporating waveform characteristics (e.g.,[97-99]).

Anderson [99] introduced a GOF framework that classifies fit quality through statistical analysis of synthetic seismograms and differences between the horizontal components of recorded seismograms. This framework employs ten comparison metrics (C_i) to evaluate and quantify the fit between observed and synthetic waveforms over a broad frequency range. These metrics include:

- C1 - Arias duration
- C2 - Energy duration
- C3 - Arias intensity
- C4 - Energy integral
- C5 - Peak acceleration
- C6 - Peak velocity
- C7 - Peak displacement
- C8 - Response spectrum
- C9 - Fourier amplitude spectrum
- C10 - Cross-correlation

Each metric is scored on a scale from 0 to 10, where a score of 10 indicates a perfect match between observed and synthetic signals for that specific metric. An overall GOF score is calculated by averaging the individual scores across all metrics and frequency bands. Anderson's scoring system categorizes the results into four fit levels: poor (<4), fair (4–6), good (6–8), and excellent (>8).

In this study, Anderson's GOF methodology was adopted to evaluate the fit between observed and synthetic waveforms, with the exception of the C10 parameter. Excluding C10 stems from challenges in ensuring consistent origin times across all records. In some cases, strong motion records lack precise start times, and uncertainties in the earthquake origin time further complicate this assumption [99]. The nine metrics used in the GOF calculation evaluate peak values, energy measures, and spectral features in both the time and frequency domains, as well as waveform shapes:

- Peak Values: Peak acceleration (C5), Peak velocity (C6) and Peak displacement (C7),
- Energy Measures: Arias intensity (C3) and the integral of velocity squared(C4),
- Spectral Features: Acceleration response spectrum (C8) and Fourier amplitude spectrum (C9),
- Waveform Shapes: Normalized integral of acceleration (C1) and Normalized integral of velocity squared (C2).

The GOF measure uses only the horizontal components of observed and synthetic earthquake records. These records are processed in the same manner as during f_c estimation, including filtering and tapering of the S-wave portions. In other words, the GOF metric is calculated for the filtered and tapered S-wave segment of the horizontal components for each earthquake.

The metrics C1 and C2 are sensitive to relative onset times between observed and synthetic waveforms. However, since the S-wave portion is used for the calculations, it is reasonable to assume that the onset times for these segments are aligned, mitigating potential discrepancies for these metrics.

For all comparisons, the observed acceleration, velocity, and displacement records are represented as $a_{obs}(t)$, $v_{obs}(t)$, and $d_{obs}(t)$. At the same time, the synthetic counterparts from simulations are denoted $a_{syn}(t)$, $v_{syn}(t)$, and $d_{syn}(t)$. Here, t ranges over the duration of strong ground motion, defined as $0 \leq t \leq T_d$, where T_d is the total duration of strong ground motions.

Similarly, the acceleration response spectra at frequency f_i are denoted as $SA_{obs}(f_i)$ and $SA_{syn}(f_i)$ for observed and synthetic records, respectively. The Fourier amplitude spectra of the observed and synthetic accelerograms at frequency f_i are represented as $FAS_{obs}(f_i)$ and $FAS_{syn}(f_i)$, respectively.

The nine different metrics used for evaluating the GOF include the following:

C1 - Arias duration (SDa)

The mathematical form of arias intensity is:

$$I_A\,(t) = \frac{\pi}{2g}\int_0^t a^2(\tau)d\tau \tag{3.29}$$

The Arias integral, as introduced by Arias [100], defines the Arias intensity IA = I_A (T_d). Arias duration is derived as:

$$N^{IA}\,(t) = \frac{I_A(t)}{IA} \tag{3.30}$$

There are many advantages and features of using Arias Intensity [99]:

- Monotonic Behavior: The metric decreases monotonically as the difference between the observed and synthetic parameters increases, ensuring consistent sensitivity to discrepancies.
- Symmetry: It provides an unbiased assessment by assigning the same score regardless of whether the observed or synthetic accelerogram exhibits the larger peak value.
- Moderation for Small Differences: Minor deviations between observed and synthetic waveforms are not penalized excessively, allowing for a more balanced evaluation.

Then, the parameter C1 is defined as:

$$F^{IA}\,(t) = \left|N_{obs}^{IA}(t) - N_{syn}^{IA}(t)\right| \tag{3.31}$$

$$C1 = \left[1 - max\left(F^{IA}\,(t)\right)\right] \tag{3.32}$$

C2 - Energy duration (SDe)

The energy associated with GM is more closely linked to the integral of velocity than to the integral of acceleration. Consequently, Anderson [99] defined the energy integral as:

$$I_E\,(t) = \int_0^t \quad v^2(\tau)d\tau \tag{3.33}$$

The total energy carried by seismic waves is proportional to IE(T_d), where the relationship incorporates the wave velocity and the density of the ground. Energy duration is subsequently expressed as:

$$N^{IE}\,(t) = \frac{I_E(t)}{IE} \tag{3.34}$$

The C2 metric for the GOF is calculated as:

$$F^{IE}\,(t) = \left|N_{obs}^{IE}(t) - N_{syn}^{IE}(t)\right| \tag{3.35}$$

$$C2 = \left[1 - max\left(F^{IE}\,(t)\right)\right] \tag{3.36}$$

C3 - Arias Intensity (SIa)

As defined in Equation (3.29), the Arias intensity represents the total energy imparted by seismic waves to the ground. This parameter is crucial for quantifying the energy release during an earthquake. The C3 metric for the GOF is calculated by comparing the Arias intensities of observed and synthetic waveforms:

$$C3 = 10\ exp\left\{-\left[\frac{(IA_{obs} - IA_{syn})}{\min(IA_{obs},\ IA_{syn})}\right]^2\right\} \tag{3.37}$$

C4 - Energy Integral (SIv)

The energy integral, detailed in Equation (3.33), quantifies the cumulative energy carried by seismic waves based on velocity over time. The C4 metric for the GOF evaluates the agreement between the observed and synthetic energy integrals. The C4 metric is:

$$C4 = 10\ exp\left\{-\left[\frac{(IE_{obs} - IE_{syn})}{\min(IE_{obs},\ IE_{syn})}\right]^2\right\} \tag{3.38}$$

C5 - Peak Ground Acceleration (Spga)

PGA is a fundamental metric for characterizing GM intensity [101] and serves as a general predictor of damage to smaller structures. PGAs are also used to approximate peak spectral acceleration for very short periods [93].

The C5 metric for the GOF is calculated by comparing the observed and synthetic PGAs:

$$A = \max|a(t)| \tag{3.39}$$

$$C5 = 10\ exp\left\{-\left[\frac{(A_{obs}-A_{syn})}{\min(A_{obs},\ A_{syn})}\right]^2\right\} \tag{3.40}$$

C6 - Peak Ground Velocity (Spgv)

PGVs are widely utilized for quantifying GMs and predicting potential damage to mid-rise structures. PGVs have been shown to correlate with intensity measures in regions such as Japan [93], [101].

The C6 metric for the GOF is:

$$V = \max|v(t)| \tag{3.41}$$

$$C6 = 10\ exp\left\{-\left[\frac{(V_{obs}-V_{syn})}{\min(V_{obs},\ V_{syn})}\right]^2\right\} \tag{3.42}$$

C7 – Peak Ground Displacement (Spgd)

PGDs serve as a critical parameter for quantifying GMs and predicting damage to large structures, such as tall buildings or bridges ([93], [102]).

The C7 metric for the GOF is determined by comparing the observed and synthetic PGDs:

$$D = \max|d(t)| \tag{3.43}$$

$$C7 = 10\ exp\left\{-\left[\frac{(D_{obs}-D_{syn})}{\min(D_{obs},\ D_{syn})}\right]^2\right\} \tag{3.44}$$

C8 - Response Spectra (Ssa)

The Response Spectra (C8) metric evaluates GM in the spectral domain and is particularly relevant for frequency-dependent structural analyses. The elastic acceleration response spectrum serves as a fundamental measure for estimating the potential intensity of seismic impacts on structures [103].

For this metric, the acceleration response (SA) with %5 damping is considered. The response spectrum can be computed at a wide range of frequencies, making it suitable for examining the dynamic behavior of different structural systems under seismic loading.

The relevant periods were selected by adding certain periods to the NGA [104] relationships. The periods considered range from 0.1 seconds to 10 seconds, reflecting both short-period and long-period responses. The selected periods are: T: 0.1s, 0.11s, 0.12s, 0.14s, 0.16s, 0.18s, 0.2s, 0.23s, 0.25s, 0.27s, 0.29s, 0.3s, 0.34v, 0.38s, 0.4s, 0.45s, 0.5s, 0.55s, 0.6s, 0.65s, 0.7s, 0.75s, 0.80s, 0.85s, 0.90s, 0.95s, 1.0s, 1.1s, 1.3s, 1.5s, 1.8s, 2.0s, 2.4s, 2.7s, 3.0s, 3.4s, 3.8s, 4.0s, 4.4s, 4.8s, 5.0s, 5.4s, 5.8s, 6.0s, 6.5s, 7.0s, 7.5s, 8.0s, 9.0s, and 10.0s.

The low-period (0.1s) and high-period (10.0s) values depend on the cut-off frequencies used for the respective earthquake couples under study.

To assess the agreement between observed and synthetic waveforms, average values are calculated over specific period intervals such as [0.1 s and 0.2 s], [0. 2 s and 0.5 s], [0. 5 s and 1.0 s], [1.0 s and 2.0 s], [2.0 s and 4.0 s], [4.0 s and 6.0 s] and [6.0 s and 10.0 s].

For each of these seven intervals, the spectral score (Ssa) is computed.

$$S_{sa}(f_i) = 10\ exp\left\{-\left[\frac{(SA_{obs}(f_i) - SA_{syn}(f_i))}{\min(SA_{obs}(f_i),\ SA_{syn}(f_i))}\right]^2\right\} \tag{3.45}$$

The C8 metric is then obtained by calculating the arithmetic average of the Ssa values:

$$C8 = \frac{\sum Ssa}{7} \tag{3.46}$$

C9 - Fourier Spectra (Sfs)

Intensity measures for strong ground motions have been shown to correlate closely with specific frequency bands within the Fourier amplitude spectrum (e.g., [105]). This metric evaluates the consistency between observed and synthetic waveforms by comparing their FAS over a range of frequency intervals.

To examine the agreement between observed and synthetic waveforms, average values are calculated across the following frequency bands: [0.1 Hz and 0.2 Hz], [0. 2 Hz and 0.5 Hz], [0. 5 Hz and 1.0 Hz], [1.0 Hz and 2.0 Hz], [2.0 Hz and 4.0 Hz], [4.0 Hz and 6.0 Hz] and [6.0 Hz and 10 Hz].

Unlike the SA metric, which focuses on specific period values within each cluster, this analysis considers all frequency values within each interval.

For each of the seven frequency intervals, a spectral Fourier score (Sfs) is calculated.

$$S_{fs}(f_i) = 10\ exp\left\{-\left[\frac{(SF_{obs}(f_i) - SF_{syn}(f_i))}{\min(SF_{obs}(f_i),\ SF_{syn}(f_i))}\right]^2\right\} \tag{3.47}$$

The final C9 metric is obtained by averaging the Sfs scores across all intervals.

$$C9 = \frac{\sum Sfs}{7} \tag{3.48}$$

This systematic and quantitative approach ensures a robust assessment of the consistency between observed and synthetic ground motions, facilitating accurate validation of simulation results.

Each metric, C1 through C9, evaluates different aspects of the waveforms, such as duration, energy, peak values, and spectral characteristics, ensuring a comprehensive comparison between the observed and synthetic signals. The GOF value for the observed and synthetic waveforms across the broadband frequency range is determined as follows:

$$GOF = \frac{\sum_{i=1}^{9} C_i}{9} \tag{3.49}$$

4. ANALYSES AND RESULTS

In the preceding chapter, the scientific foundation and mathematical framework for GM simulation methods, including f_c estimation and the EGF method, were thoroughly explained. Building on that foundation, this chapter presents the analysis results for 11 medium-sized earthquakes along the EAFZ. The focus is on the practical implementation of these methodologies and the interpretation of their outcomes.

Section 4.1 begins by outlining the initial parameters essential for estimating corner frequencies, along with a detailed explanation of the step-by-step spectral analysis process.

In Section 4.2, a comprehensive framework is presented to illustrate the initial parameters, procedural steps, and outcomes of simulations conducted using the EGF method.

4.1. Corner Frequency (f_c) Estimation Results

This section focuses on the critical source scaling parameters required for EGF simulations: C and N. These parameters are derived by determining the f_c from the source spectra of 10 medium-sized earthquakes (Mw >5) and their corresponding 10 aftershocks, which have occurred along the EAFZ since 2020.

The analysis utilizes a comprehensive dataset comprising approximately 172 FAS of S-waves recorded by 86 strong ground motion stations. This extensive dataset facilitates a robust spectral analysis, ensuring accurate f_c estimation and the reliable derivation of scaling parameters required for EGF simulations. Estimating f_c from the source spectrum includes the following steps:

Acquisition of Earthquake Records: For the earthquake couples identified in Section 2.2, raw earthquake records from selected strong ground motion stations (see Table 4.1) are required.

Horizontal Component Analysis: The analysis focused exclusively on the horizontal components (NS and EW) of the GM recordings. A 16-second time window was utilized to

identify noise segments, while the S-wave portion was extracted using the same time window, starting 1 second before and ending 15 seconds after the S-wave arrival. To avoid missing S-starts, data initialization began 1 second prior to the S-wave start.

Determining the Filter Ranges: The FAS of the S-wave and noise portions for each earthquake were computed to establish appropriate filter ranges. The filter range, in other words cut-off frequency (fcut-off), was identified as the range where the S-wave FAS exceeded the noise FAS by a factor of at least three. For this study, the low-frequency cut-off (f_{min}) was set to 0.1 Hz, while the high-frequency cut-off (f_{max}) was limited to 10 Hz. When estimating the fc of an earthquake, the maximum f min and the minimum f max values across all stations were used.

Filter and Taper Records: Earthquake records were acasually filtered using a second-order band-pass filter, applied according to the fcut-off values, which are determined considering the signal-to-noise ratio (SNR). A new S-wave window was selected from the filtered earthquake recordings, and a 10% cosine taper was applied to smooth the edges. This tapering gradually reduced the first and last 5% of the selected records to zero, ensuring smoother transitions.

Calculation and Normalization of FAS: The FAS for the filtered and tapered S-wave segments of each earthquake was calculated. The geometric average of the $FAS_{EW\text{-}NS}$ values for the East-West (FAS_{EW}) and North-South (FAS_{NS}) horizontal components was calculated to represent the overall spectral characteristics of the earthquake.

$$FAS_{EW-NS} = \sqrt{FAS_{EW}\ \ FAS_{NS}} \tag{4.1}$$

To account for geometric spreading effects, each $FAS_{EW\text{-}NS}$ was normalized by multiplying it with the R_{epi}.

Generation of the Source Spectrum: The source spectrum was generated by taking the logarithmic average of the normalized FAS across all stations for each earthquake. The f_c was subsequently estimated by fitting the Brune point source model (see Figure 3.1) to the observed mean spectrum.

This systematic approach ensures precise estimation of the f_c, forming a foundation for accurate EGF simulations. Table 4.1 presents the cut-off frequency limits applied to the

Table 4.1. Corner frequency (f_c) estimation as a result of Spectral Analyses.

Earthquake No	Magnitude (Mw)	Stations (section 2.1.2.1)	Range of analyses Hz	fc Hz
1 m	6.80	0205-0207-0212-2104-2302-2304-4401-4404-4407-6201	0.10-10	0.13
1 a	5.00	0205-0207-0212-2104-2302-2304-4401-4404-4407-6201	0.10-10	0.51
2 m	5.10	0212-2104-2302-2307-4404-4407-4412-6201	0.15-10	0.98
2 a	4.40	0212-2104-2301-2302-2307-4404-4407-4412-6201	0.15-10	1.85
3 m	5.60	0205-0212-2107-2309-4405-4406-4408-4411-4412	0.15-10	0.25
3 a	4.70	0205-0212-2107-2309-4404-4405-4406-4408-4411-4412	0.15-10	1.02
4 m	5.60	0213-2107-2305-2409- 2415-2711-4405-4406-4614-4631-6201-6302	0.20-10	0.25
4 a	4.40	0213-2107-2309-2409-2415-2711-4404-4409-4410-4412-4631-6302	0.20-10	1.27
5 m	5.60	0201-0204-0205-0212-2104-2105-2302-2305-2307-2309-2408-2409-2415-4404-4405-4406-4412-6201	0.40-10	0.63
5 a	4.30	0204-2107-2301-2302-2307-2308-2309-2409-4404-6201	0.40-10	1.85
6 m	5.20	2309-2310-2710-2713-2714-4404-4413-4414	0.40-10	0.93
6 a	4.10	2309-2310-2710-2713-2714-4404-4413-4414	0.40-10	1.78
7 m	5.40	0205-0213-2310-2703-2710-2711-2712-4409-4410-4412-4611-4614-4617-4618-4624-4625-6303	0.30-10	0.82
7 a	4.00	0205-0213-2310-2703-2710-2711-2712-4404-4405-4410-4412-4611-4614-4615-4617-6303	0.30-10	2.15
8 m	5.30	0122-0127-0129-2703-2711-3804-4405-4409-4410-4412-4611-4613-4614-4615-4617-5807-6304	0.40-10	0.95
8 a	4.00	0122-0127-0129-2703-2711-4405-4409-4410-4412-4611-4613-4614-4615-4617-5807-6304	0.40-10	2.58
9 m	6.30	0120-0130-2703-2711-3115-3116-3134-3303-3304-3305-4613-4615-4617-8003-8004	0.20-10	0.68
9 a	4.80	0120-0130-2703-2711-3115-3116-3134-3135-3146-3147-3303-3304-3305-4613-4615-4617-8003-8004	0.20-10	1.27
10 m	5.80	0118-0119-0120-0122-0125-0127-0128-0129-0130-2704-2711-2712-2718-3305-3805-4615-4617-8002-8003-8004	0.25-10	0.85
10 a	4.40	0120-0122-0125-0127-0129-0130-2704-2711-2712-2718-3802-4615-4617-4624-8003-8004	0.25-10	2.15
11 m	6.70	*	0.20-10	*
11 blind	5.00	*	*	*
11 a	4.00	*	0.20-10	*

4.2. Simulation Results

GM simulations for the target earthquakes were performed using the EGF method to estimate the SMGA. These simulations utilized acceleration, velocity, and displacement records from multiple stations surrounding the epicenters of the mainshocks and their aftershocks (see Figure 2.3 to Figure 2.16).

The source scaling parameters for earthquake couples, whose corner frequencies were derived through spectral analysis, were calculated using Equation (3.27) and Equation (3.28). Consequently, the initial values for critical parameters, including N and C, as well as the V_s and V_r, are presented in Table 4.2. The average V_s and V_r near the hypocenter were determined to be 3.5 km/s and 2.8 km/s, respectively. The V_s-V_r conversion was performed using Equation (3.18).

Additional source parameters necessary for the simulations were collected from existing literature (see Table 2.14). Furthermore, the filtering intervals for the EGF simulations were adopted from the values used during the f_c estimation process. These values serve as the initial input for conducting the EGF simulations.

Table 4.2. Initial parameters used in the simulation.

Earthquake No	Magnitude (Mw)	Mo/mo values	fcm Hz	fca Hz	Range of analyses Hz	N	C	Vs (km/sn)	Vr (km/sn)
1 m / 1 a	6.8/5.0	272.73	0.13	0.51	0.10-10	4.00	4.00	3.50	2.80
2 m / 2 a	5.1/4.4	8.28	0.98	1.85	0.15-10	2.00	1.00		
3 m / 3 a	5.6/4.7	23.50	0.25	1.02	0.15-10	4.00	1.00		
4 m / 4 a	5.6/4.4	63.10	0.25	1.27	0.20-10	5.00	1.00		
5 m / 5 a	5.6/4.3	89.13	0.63	1.85	0.40-10	3.00	2.50		
6 m / 6 a	5.2/4.1	44.67	0.93	1.78	0.40-10	2.00	5.50		
7 m / 7 a	5.4/4.0	125.89	0.82	2.15	0.30-10	3.00	4.50		
8 m / 8 a	5.3/4.0	89.13	0.95	2.58	0.40-10	3.00	3.30		
9 m / 9 a	6.3/4.8	170.49	0.68	1.27	0.20-10	3.00	5.00		
10 m / 10 a	5.8/4.4	125.89	0.85	2.15	0.25-10	3.00	5.00		
11 m / 11 blind	6.7/5.0	354.81	*	*	0.20-10	*	*		
11 blind / 11 a	5.0/4.0	31.62	*	*	0.20-10	*	*		

calculated for each station based on the acceleration waveforms. The time difference between these arrivals was determined, and the S-wave portion, or the S-wave time window, was defined as three times this difference, a standard widely referenced in the literature. Next, a 10% cosine taper was applied to the edges of the selected S-wave window to smooth transitions and minimize abrupt changes in the waveform. Lastly, the FAS was computed for the filtered and tapered S-wave segments for each earthquake.

It is known that simulations performed by adhering to source scaling relationship parameters give the best and most accurate results. However, due to the lack of region-specific parameters during f_c estimations for calculating N and C, certain values, such as Q (f) and κ, along with their associated exponential terms, were omitted (see Equation (3.14)). Additionally, the f_c estimation was performed visually using the Brune source model, which may introduce errors due to the subjective nature of visual readings and the absence of specific regional parameters.

To address these uncertainties, alternative N parameter values (N±1) were evaluated alongside corresponding C values recalculated for each adjusted N. For instance, in simulations where N 4 was used, all possible subfault division combinations were tested: 3x3, 3×4, 3×5, 4×3, 4×4, 4×5, 5×3, 5×4, and 5×5. In these combinations, the first number represents the number of subfaults along the strike direction, and the second number represents the number of subfaults along the dip direction. Different C values were applied for each alternative to refine the simulations.

The SMGA size, positional parameters, and RT were determined by selecting the model with the best GOF between the observed and simulated ground motion.

Table 4.3 and Figure 4.3 illustrate the nine GOF metric values calculated for each station for the 2nd earthquake couple. For the remaining earthquake pairs, the GOF metric values for all stations are provided in Appendix A.

In Table 4.3, the GOF value for each station is calculated separately for the E-W and N-S components. The arithmetic mean of these values is then determined to provide a single GOF value for each station. Subsequently, the average of all the station-specific GOF values is computed, yielding the overall GOF value that reflects the simulation's accuracy for the given earthquake couples.

For this example, the overall GOF value is calculated as 8.14. According to the GOF criteria, a value between 8 and 10 indicates an excellent simulation. Consequently, the SMGA, RT, and RSP parameters that produce this GOF value are identified as the source parameters for this earthquake. Waveforms for all earthquake couples are included in Appendix B.

The source parameters for the small events of each earthquake couple are summarized in Table 4.4.

Table 4.4. The source parameters for the aftershock from forward EGF simulation.

Num	Mw	Rise Time (s)	SMGA (km2) (Str. x Dip)
1 a	5.00	0.16	2.60 x 2.60
2 a	4.40	0.08	1.80 x 1.00
3 a	4.70	0.08	0.80 x 2.40
4 a	4.40	0.08	1.00 x 0.80
5 a	4.30	0.08	1.60 x 1.00
6 a	4.10	0.16	1.60 x 1.80
7 a	4.00	0.08	2.60 x 0.80
8 a	4.00	0.06	1.20 x 2.00
9 a	4.80	0.08	2.40 x 2.60
10 a	4.40	0.08	1.20 x 1.80
11 a	4.00	*	*
11 blind	5.00	*	*

The lower limit for the RT was set at 0.08 seconds for all earthquakes analyzed in this study. However, for the 8th earthquake couple, the variation in the GOF was specifically evaluated at an RT value of 0.06 seconds. Based on this evaluation, the RT value for the 8th earthquake couple was adjusted to 0.06 seconds to achieve improved simulation accuracy.

To estimate the source parameters for the large earthquakes, the parameters in Table 4.4 were scaled using the fault dimension ratio (N) between the earthquake couples. The calculated parameters for the large earthquakes are presented in Table 4.5.

Table 4.5. The source parameters for the mainshock from foward EGF simulation.

Num	Mw	N (Str. x Dip)	C	Rise Time (s)	RSP* (Str. x Dip)	SMGA (km2) (Str. x Dip)	GOF
1 m	6.80	5 x 4	3.4	0.80	1 x 1	13.0 x 10.4	7.22
2 m	5.10	2 x 2	1.1	0.16	2 x 2	3.60 x 2.00	8.14
3 m	5.60	5 x 4	0.8	0.40	1 x 1	4.00 x 9.60	7.86
4 m	5.60	5 x 6	0.9	0.48	1 x 4	5.00 x 4.80	7.95
5 m	5.60	4 x 4	3.0	0.32	1 x 2	6.40 x 4.00	6.70
6 m	5.20	3 x 2	3.3	0.48	1 x 2	4.80 x 3.60	7.98
7 m	5.40	4 x 3	2.3	0.32	3 x 1	10.4 x 2.40	7.50
8 m	5.30	3 x 3	2.4	0.18	1 x 2	3.60 x 6.00	7.80
9 m	6.30	3 x 4	4.1	0.32	3 x 1	7.20 x 10.4	8.19
10 m	5.80	4 x 3	4.5	0.32	1 x 1	4.80 x 5.40	8.08
11 m	6.70	*	*	*	*	*	*
11 blind	5.00	*	*	*	*	*	*

As detailed in Table 4.4 and Table 4.5, the source parameters for the 11th earthquake pair could not be determined. This is due to the need for an artificial Mw 5.0 earthquake, which must be generated using the records of the Mw 4.0 earthquake. Subsequently, the source parameters for the Mw 6.7 earthquake will be derived using the records of the generated Mw 5.0 earthquake. However, during the first stage of this process, while attempting to derive the source parameters for the Mw 5.0 earthquake from the Mw 4.0 event, no records are available for the Mw 5.0 earthquake. Consequently, f_c estimation and source scaling parameters could not be established. To address this issue, a blind EGF simulation will be employed to generate the source parameters for the Mw 5.0 earthquake from the Mw 4.0 aftershock.

4.2.1. Blind EGF Simulation for 11th Eaarthquake Couple

4.2.1.1. Generating the artificial earthquake of Mw 5.0 with the 2015 Mw 4.0 Kahramanmaraş earthquake (11a).

This section focuses on estimating records for an artificial Mw 5.0 earthquake through blind EGF simulation. Two critical parameters, N and C, are required for the simulation. These parameters are determined as follows:

N, Fault Dimension Scaling Parameter: The primary purpose of the N parameter is to scale the dimensions of the SMGA from the aftershock to the mainshock. The SMGA dimensions for the large earthquake are determined by multiplying the dimensions of the small earthquake's SMGA by N in the strike and dip directions. If the SMGA of the large earthquake is considered square, the following relationship is used:

$$N^2 = \frac{LL\ LW}{ll\ \ lw} \tag{4.2}$$

where, LL and LW are SMGA dimensions for the larger earthquake while ll and lw are SMGA dimensions for the smaller earthquake.

Past observations indicate that the SMGA of small earthquakes typically equals the RA. Using theoretical and empirical SMGA estimates, the N parameter can be determined.

The theoretical relationship provided by Somerville et al. [43]:

$$RA = 2.23\ 10^{-15}.\ {M_o}^{2/3} \tag{4.3}$$

where, the unit of M_o is dyne. cm. The M_o for a Mw 5.0 earthquake corresponds to an SMGA of 11.18 km², while a Mw 4.0 earthquake corresponds to 1.12 km². When Equation (4.2) is applied the value of N is approximately 3.

Based on the Wells and Coppersmith [106]:

$$RA = -3.42(\pm 0.18) + 0.90(\pm 0.03)\ M_w \tag{4.4}$$

where, average values were used. The SMGA is estimated at 11.89 km² for the larger earthquake and 1.50 km² for the smaller earthquake. When Equation (4.2) is applied, the N parameter can range from 2 to 3.

C, Stress Drop Scaling Parameter: Using Equation (3.25), the C parameter is calculated for each simulation. Initial values such as N=2×2, N=2×3, N=3×2, and N=3×3

are combined with corresponding C values, and blind EGF simulations are conducted to identify the most accurate parameters.

The blind EGF simulation follows the methodology outlined in Section 4.2.1. Since no records are available for the mainshock, the simulation process incorporates region-specific predictive models, such as the PGV model developed by Kuran et al. (KTP24) [107]. This model predicts PGV values for Turkiye based on specific seismic parameters.

Input Parameters for KTP24 [107]:

- Mw and Dip angle: Taken from Table 2.14
- Vs30 value: The Vs30 value is taken as the basis at the station where the PGV value is sought.
- The epicentral distance (R_{epi}): Provided by AFAD
- Joyner-Boore distance (R_{JB}) and rupture distance (R_{rup}): Taken directly from Sandikkaya et al. [108].

Using the KTP24 model [107], PGV values for the desired locations were calculated and are presented in Table 4.6.

Table 4.6. The Preticted PGV values from KTP24.

Station	Mw	Dip (^{o})	Vs30 (m/s)	R_{jb} (km)	R_{rup} (km)	R_{epi} (km)	KTP24-PGV cm/s
122	5.00	48	501	103.00	104.00	103.00	0.10720
2704			721	80.00	80.00	80.00	0.10720
2705			720	44.00	45.00	44.00	0.35308
3138			619	68.00	68.00	68.00	0.19330
3142			538	103.00	104.00	103.00	0.10720
4408			654	120.00	121.00	120.00	0.09997
4614			541	36.00	37.00	36.00	0.47907
4615			485	18.00	19.00	18.00	1.42136
4617			574	35.00	36.00	35.00	0.47907
4619			545	34.00	35.00	34.00	0.47907
4621			714	34.00	35.00	34.00	0.47907
4623			561	31.00	32.00	31.00	0.47907
7901			463	66.00	66.00	66.00	0.21566
8002			430	38.00	39.00	38.00	0.50003

Table 4.7. Source parameter models of Mw 5.0 earthquake calculated according to minimum residual values.

Model No	N	C	LL (km)	LW (km)	RT (s)	RSP (Str. x Dip)
1	2 x 3	2.6	3.6	3.0	0.24	2 x 1
2	3 x 2	2.6	3.0	2.4	0.24	3 x 1
3	3 x 2	2.6	2.4	2.8	0.24	3 x 1
4	3 x 2	2.6	3.0	3.2	0.24	3 x 1
5	3 x 2	2.6	3.0	3.6	0.24	3 x 1
6	3 x 2	2.6	3.6	2.0	0.24	3 x 1

The values given in Table 4.7 are the values produced for the Mw 5.0 mainshock as a result of the EGF simulation. These selected parameters constitute the aftershock data for accurate modeling of the Mw 6.7 earthquake. A schematic comparison of the PGV values generated from simulations, calculated according to the minimum residual values for the Mw 5.0 earthquake, and the PGV values derived from the KTP24 model [107] is presented in Appendix C.

4.2.1.2. Estimation of source parameters for the 2023 Mw 6.7 Gaziantep earthquake (11 m) with the Mw 5.0 artificial earthquake.

This section focuses on deriving the source parameters for the Mw 6.7 earthquake.

As previously mentioned, due to the lack of a defined f_c for the Mw 5.0 earthquake and the absence of a single best-fitting model in Section 4.2.1.1, the N and C parameters were estimated by proportioning the theoretically calculated SMGA values of the mainshock and its aftershock.

Calculating SMGA Using Somerville et al. [43]:

First, the RA for the mainshock and aftershock was calculated using Equation (4.3). According to Somerville et al., for large earthquakes, the SMGA is approximately 22% of the RA. The RA for the mainshock was determined to be 560.15 km², and 22% of this value yielded an SMGA of 123.23 km². For the aftershock, SMGA and RA were assumed to be equal, resulting in an SMGA of 11.18 km². Using Equation (4.2) to proportion the areas of the earthquake pair, the N value was found to range between approximately 3 and 4.

Calculating SMGA Using Wells and Coppersmith [106]:

Following the same procedure with Equation (4.4), the RA for the mainshock was calculated as 402.72 km², leading to an SMGA of 80.60 km² for the large earthquake. For the small earthquake, the SMGA was calculated to be 11.89 km². From these values, the N parameter was determined to be 3.

Model-Based Calculations:

Using the SMGA values for the aftershock from the six models outlined in Table 4.7, the SMGA for the mainshock was proportioned to the SMGA of the aftershock. Mainshock SMGA values: (1) according to Somerville's model, the SMGA of the mainshock was 123.23 km², while (2) Wells and Coppersmith's model calculated it as 80.60 km². Based on these models, the N parameter varied between 3, 4, and 5.

Using the three different calculations above, all combinations of N values (3, 4, and 5) were tested. For each combination, the C parameter was calculated using Equation (3.25). As observed records of the Mw 6.7 earthquake were available, the best GOF value was sought for each model by varying the N and C values.

The optimal GOF value was achieved by selecting aftershock parameters from Model 2 (see Table 4.7), leading to the generation of source parameters for the mainshock. The best GOF value was determined to be 7.41, with N set to “5 x 4” and C set to “3.5”. Consequently, Model 2 was identified as the best-fitting model for the aftershock.

The Mw 4.0 earthquake was simulated using the Mw 5.0 earthquake as the Green's function (refer to Section 4.2.1.1). The fit between the observed and synthetic data was evaluated based on the PGV criterion. Using this fit criterion, the source parameters for both the mainshock and the aftershock, as determined from Model 2, which provided the best fit, are presented in Table 4.8.

Table 4.8. Source parameters of Mw 4.0 and Mw 5.0 earthquakes.

Num	Mw	N (Str. x Dip)	C	Rise Time (s)	RSP* (Str. x Dip)	SMGA (km2) (Str. x Dip)	GOF
11 blind	5.00	3 x 2	2.60	0.24	3 x 1	3.0 x 2.4	*
11 a	4.00			0.08		1.0 x 1.2	

Similarly, the source parameters for the Mw 6.7 mainshock were derived using waveforms from the artificially generated Mw 5.0 earthquake. As observed records of the Mw 6.7 earthquake were available, the analysis was completed by identifying the model with the highest GOF parameter between the observed and synthetic data. The source parameters for the Mw 6.7 mainshock are summarized in Table 4.9.

Table 4.9. Source parameters of Mw 6.7 earthquake calculated according to highest GOF values.

Num	Mw	N (Str. x Dip)	C	Rise Time (s)	RSP* (Str. x Dip)	SMGA (km2) (Str. x Dip)	GOF
11 m	6.70	5 x 4	3.50	1.20	1 x 1	15 x 9.6	7.41
11 blind	5.00			0.24		3.0 x 2.4	

Additionally, a comprehensive table detailing the GOF metrics for the Mw 6.7 earthquake is included in Appendix A. The observed and synthetic waveforms resulting from the Mw 6.7 earthquake simulation are provided in Appendix B.

4.2.2. Stress Drop (Δσ) Results

Δσ refers to the difference in stress levels on a fault before and after an earthquake rupture occurs. Understanding the properties of stress release during an earthquake is essential for accurately modeling seismic sources in both probabilistic and deterministic seismic hazard assessments. For a circular source model, Δσ can be estimated using Brune's [3], [69] formula:

$$\Delta\sigma = \frac{7}{16}\frac{M_o}{r^3} \tag{4.6}$$

where, M_o is the seismic moment, and r represents the radius of the circular asperity area.

As seen in Equation (4.6), Δσ is proportional to the cube of the characteristic fault dimension, emphasizing the importance of accurately determining fault dimensions. Consequently, Δσ values calculated based on SMGAs, determined from the highest GOF parameter, provide the most reliable estimates for the roughness area along the fault.

Table 4.10. Estimated stress drop (Δσ) in the SMGA.

Earthquake No	Magnitude (Mw)	fc (Hz)	C	Δσ (MPa)
1 m	6.80	0.13	3.40	22.29
1 a	5.00	0.51		6.56
2 m	5.10	0.98	1.10	8.66
2 a	4.40	1.85		7.87
3 m	5.60	0.25	0.80	9.01
3 a	4.70	1.02		11.26
4 m	5.60	0.25	0.90	13.69
4 a	4.40	1.27		15.21
5 m	5.60	0.63	3.00	11.42
5 a	4.30	1.85		3.81
6 m	5.20	0.93	3.30	2.61
6 a	4.10	1.78		0.79
7 m	5.40	0.82	2.30	2.10
7 a	4.00	2.15		0.91
8 m	5.30	0.95	2.40	1.76
8 a	4.00	2.58		0.74
9 m	6.30	0.68	4.10	15.35
9 a	4.80	1.27		3.74
10 m	5.80	0.85	4.50	15.43
10 a	4.40	2.15		3.43
11 m	6.70	*	3.50	18.92
11 blind	5.00	*	2.60	5.41
11 a	4.00	*		2.08

5. DISCUSSION

5.1. Discussion of Goodness of Fit (GOF) Parameters

The source parameters for the target earthquake pairs were determined using the EGF method. The GOF value, calculated based on nine distinct metrics, served as the benchmark for identifying the most accurate source parameters. The primary objective throughout the study was identifying the source parameters that yielded the highest GOF value.

The GOF parameter provides a comprehensive assessment of earthquake records by evaluating multiple aspects, including peak values, energy measures, spectral features, and waveform shapes in both time and frequency domains.

Table 4.2 presents the initial values for the EGF simulations. Using these values as initial points, all possible combinations of SMGA size, RT, and RSP were tested to identify the parameters that produced the best GOF scores. Due to certain limitations, the estimation of N and C parameters may involve some inaccuracies. To address these, the analysis was iteratively repeated across various combinations of N and C values, ensuring the best GOF results were achieved.

The simulation results, after repeated analyses, are summarized in Table 4.5 and Table 4.9, which highlight changes in source parameters for all earthquake couples corresponding to the highest GOF values. Detailed changes in GOF metrics between observed and synthetic data at each station and for each direction (E-W and N-S) are provided in Appendix A.

Figure 5.1 illustrates the average GOF metrics calculated for each station and the horizontal component (E-W and N-S), while Figure 5.2 provides a bird's-eye view of the same data. For the 11th earthquake couple, the evaluation of GOF values is valid only for the Mw 6.7 (11 m) earthquake, and Figure 5.1 and Figure 5.2 specifically highlight the results for this couple.

ranges; however, it is more affected by high-frequency components due to its dependence on the squared of acceleration.

The sensitivity of Arias Intensity, both scatterings and sudden peaks in acceleration, can lead to lower values for this metric. Furthermore, the EGF method is more adept at capturing medium- to low-frequency content than high-frequency components. Consequently, Arias Intensity may have underperformed in this context. In contrast, metrics that emphasize medium-frequency content (Spgv) and low-frequency components (Spgd) demonstrated significantly better performance.

Finally, Appendix B provides synthetic waveforms generated based on source parameters best identified by GOF values, alongside the observed waveforms. Although minor differences are occasionally seen between the observed and synthetic waveforms during visual inspection, the overall agreement is generally good, with some stations exhibiting almost perfect agreement.

5.2. Discussion of Source Characterization for Broadband GM Simulation

The source parameters for 11 moderate-sized earthquakes along the EAFZ were determined through simulations utilizing the EGF method. Optimal source parameters were identified by evaluating combinations of SMGA dimensions, RT, RSP, and scaling parameters N and C. The parameters yielding the highest GOF values were selected as the most accurate source parameters and are summarized in Table 4.5, Table 4.8, and Table 4.9.

The GOF metric exhibited greater sensitivity to RSP and SMGA dimensions than to RT. While small changes of 0.02 seconds in RT caused negligible variations in GOF values, even slight adjustments in RSP and SMGA dimensions significantly impacted GOF outcomes.

Figure 5.3 compares the source parameters derived in this study with scaling relationships proposed by Somerville et al. [43] and Wells and Coppersmith [106].

Figure 5.6 illustrates the relationship between RT and M_o for the SMGA. Here, RT is defined as the duration of the filtering function F (t). The RT values derived in this study are distributed around the relationship proposed by Somerville et al. [43]. Similar distributions are observed in the findings of Tanircan's [62] and Miyake's [42].

In regions where $M_o \approx 1\times10^{22}$, RT values derived in this study are systematically higher than those suggested by Somerville et al. [43]. This discrepancy may arise from the constraint of limiting RT to 0.08 seconds during the simulation phase. High RT values for small earthquakes could also lead to an overestimation of RT for the mainshocks.

The effect of RT on PGV is significant: increasing RT reduces PGV, while decreasing RT increases PGV. Therefore, beginning simulations with lower RT values enhances the accuracy of PGV predictions.

Finally, it was observed that abrupt changes in the RT values have a substantial impact on the GOF parameter and the overall simulation results. In contrast, minor increases in the RT value result in slight variations in the simulation outcomes and GOF scores. This finding is supported by numerous studies, including those conducted by Miyake et al. [42] and Tanircan et al. [62].

5.3. Discussion of Stress Drop

RT, V_r, RSP, and $\Delta\sigma$ are among the most critical parameters influencing variations in ground shaking intensity. High-frequency GM is primarily governed by $\Delta\sigma$, which significantly affects PGA and its attenuation. A decrease in $\Delta\sigma$ reduces both PGA and PGV, while an increase in $\Delta\sigma$ results in higher values for both. Therefore, accurately estimating $\Delta\sigma$ is of paramount importance for understanding GM characteristics.

The most suitable source parameters for each earthquake couple were determined based on the highest GOF values from simulations conducted using the EGF method. The changes in $\Delta\sigma$ for the SMGA, calculated using these source parameters, are summarized in Table 4.10. These stress drop values are visually represented in Figure 5.7.

$$\Delta\sigma = \frac{7}{16}\frac{M_o}{r^3} \quad (5.2)$$

- In contrast, Miyake et al. [42] calculate the stress drop for SMGA using the formula:

$$\Delta\sigma = \frac{7}{16}\frac{M_o}{R\,r^2} \quad (5.3)$$

Here, M_o is the seismic moment (in dyne cm), R is the equivalent radius of the RA, and r is the equivalent radius of the SMGA. For large magnitude earthquakes, the R-value is larger than the r-value; Miyake et al. [42] obtain lower Δσ values for SMGA.

For earthquakes with corner frequencies exceeding 0.3 Hz, the Δσ values reported by Tanircan et al. [62] and those determined in this study range between 1 MPa and 10 MPa, demonstrating a consistent agreement between the two studies.

Batman et al. [110] analyzed Δσ for 61 medium-sized earthquakes (Mw 4.0 to Mw 6.3) from the 2023 Kahramanmaras sequence using two methods:

- Andrew's Method yielded Δσ values ranging between 0.1 MPa and 10 MPa.
- Visual Inspection Method showed more consistent results, with Δσ values between 1 MPa and 10 MPa.

For small to medium-sized earthquakes, SMGA and RA are often considered equivalent. Since Batman et al. [110] focused on medium-sized events, their Δσ results are directly comparable to those of this study. The Δσ values derived using the Visual Inspection Method align closely with the results obtained in this study.

The findings emphasize the importance of accurate Δσ estimation and its relationship with GM parameters. The alignment of seismic gaps, Δσ distributions, and observed seismic events provides robust evidence for the reliability of the methods used in this study. Furthermore, the comparative analysis with other studies supports the validity of the results and highlights the consistency of Δσ trends across different regions and methodologies.

6. CONCLUSIONS and SUGGESTIONS

6.1. Conclusions

This study focused on generating source parameters for medium-sized earthquakes along the EAFZ, starting from the January 24, 2020 Sivrice earthquake and extending to the 2023 Kahramanmaras earthquake sequence and their aftershocks. The source parameters were determined using the EGF method, with an emphasis on obtaining the highest GOF values across nine metrics that evaluate peak values, energy measurements, spectral features, and waveform shapes in both time and frequency domains.

All GOF values exceeded 7, except for the 5th earthquake couple, which achieved a score of 6.7. A GOF score between 6 and 8 denotes good simulation quality, while scores ranging from 8 to 10 indicate excellent performance. Despite the lowest GOF value being 6.7, simulations for seven earthquake pairs were classified as "good," whereas four pairs demonstrated "excellent" simulation quality. Among the nine metrics, C6 (Spgv) and C7 (Spgd) showed the highest performance, while C3 (SIa) showed the lowest performance. The Arias Intensity metric (C3) demonstrates the lowest performance primarily due to its sensitivity to abrupt variations in the acceleration waveform and its reliance on high-frequency content.

SMGA parameters were derived through forward modeling of horizontal components (E-W and N-S) of displacement, velocity, and acceleration waveforms. Iterative simulations were conducted by varying critical aftershock source parameters such as RSP, RT, and SMGA dimensions. The combinations that yielded the highest GOF values were selected as the most accurate representations of the source parameters.

The SMGAs derived from EGF simulations in this study were compared with findings from studies conducted on earthquakes in Turkiye and globally. Overall, the results demonstrate a high degree of consistency with previously reported SMGAs. Additionally, the SMGAs obtained in this study predominantly fall between the RA trend line and the combined asperity area trend line derived from source scaling relationships. For this reason,

this study proposed a new M_o-SMGA scaling relationship tailored to the EAFZ, which was validated by blind EGF simulations. The SMGAs determined using the two-stage compatibility approach, based on PGV and GOF metrics, align closely with the proposed trend, thereby validating the newly established SMGA-M_o relationship.

The 2023 Mw 6.3 Hatay earthquake was modeled using waveform inversion to determine its slip distribution and simulated with the EGF method under the assumption of a single SMGA (9m/9a). Both approaches yielded consistent results, demonstrating the reliability and robustness of the EGF method for accurately modeling seismic events.

The RT values obtained in this study closely align with established scaling relationships, exhibiting patterns consistent with those observed in prior research. These findings reaffirm the reliability of the derived RT values and their agreement with existing source scaling models. However, it is noteworthy that the RT values for smaller earthquakes were significantly higher. This discrepancy arises from the lower limit of the RT value being constrained to 0.08 in the EGF simulations. Moreover, small variations in RT resulted in only minor changes to simulation outcomes and GOF scores, a finding consistent with prior studies.

$\Delta\sigma$ values for the EAFZ range from 0.74 MPa to 22.29 MPa. Among the fault segments examined, the Pazarcik Segment exhibited the lowest $\Delta\sigma$ values, while the Puturge Segment showed significantly higher $\Delta\sigma$. The stress drop ratio in some earthquake couples in the Puturge segment is close to 1.0, suggesting considerable stress accumulation in this region. Additionally, a potential seismic gap was identified in the Puturge Segment, corresponding to areas of high-stress accumulation. This seismic gap aligns with regions identified as unruptured during the 2020 Sivrice and 2023 Kahramanmaras earthquake sequences. The occurrence of an Mw 5.9 earthquake on October 16, 2024, within this seismic gap validated the stress-loaded region identified in this study.

For corner frequencies between 0.1 and 0.3 Hz, $\Delta\sigma$ values from this study exceeded 10 MPa, while other studies reported lower values due to differences in modeling approaches. For corner frequencies above 0.3 Hz, $\Delta\sigma$ values ranged from 1 MPa to 10 MPa, showing strong consistency with prior findings. Analyses conducted using alternative methods following the 2023 Kahramanmaras earthquake sequences yielded $\Delta\sigma$ values closely aligning with those reported in this study.

6.2. Suggestions

- The EGF method demonstrates the potential for generating large earthquake simulations using records of small events, especially in regions where mainshock records are unavailable or contain high noise levels.
- Relocation of earthquake epicenters can enhance the precision of source parameter estimates and GOF values.
- Region-specific Vs and Vr values should be incorporated to refine results.
- Reducing the minimum RT value from 0.08 s could improve accuracy for small earthquakes and better align with observed values.
- Incorporating regional K and Q (f) values during corner frequency estimation can lead to more reliable spectral analyses and source scaling parameters.
- The Mo-SMGA scaling relationship proposed for the EAFZ provides a critical framework for understanding rupture dynamics and can inform seismic hazard models in the region.
- Data from multiple institutes were utilized in this study; however, for consistency, it is recommended to rely solely on the data from a single institute.

REFERENCES

1. Kanamori, H., and E. E. Brodsky, “The physics of earthquakes”, *Reports on Progress in Physics*, Vol. 54, pp. 1429–1496, 2004.
2. Cotton, F., R. Archuleta, and M. Causse, “What is Sigma of the Stress Drop?”, *Seismological Research Letters*, Vol. 84, No. 1, pp. 42–48, 2013.
3. Brune, J. N., “Tectonic stress and the spectra of seismic shear waves from earthquakes”, *Journal of Geophysical Research*, Vol. 75, No. 26, pp. 4997–5009, 1970.
4. Abercrombie, R. E., “Investigating uncertainties in empirical Green's function analysis of earthquake source parameters”, *Journal of Geophysical Research Solid Earth*, Vol. 120, pp. 4263–4277, 2015.
5. Somerville, P., M. Sen, and B. Cohee, “Simulation of strong ground motions recorded during the 1985 Michoacán, Mexico and Valparaíso, Chile earthquakes”, *Bulletin of the Seismological Society of America*, Vol. 81, No. 1, pp. 1–27, 1991.
6. Irikura, K., “Semi-Empirical Estimation of Strong Ground Motions During Large Earthquakes”, *Bulletin of the Disaster Prevention Research Institute*, Vol. 33, No. 298, pp. 63–104, 1983.
7. Hartzell, S. H., “Earthquake aftershocks as Green's functions”, *Geophysical Research Letters*, Vol. 5, No. 1, pp. 1–4, 1978.
8. Boore, D. M., “Stochastic simulation of high-frequency ground motions based on seismological models of the radiated spectra ”, *Bulletin of the Seismological Society of America*, Vol. 73, No. 6A, pp. 1865–1894, 1983.
9. Irikura, K., “Prediction of strong acceleration motions using empirical Green's function”, *In Proc. 7th Japan Earthquake Engineering Sympozium*, Vol. 151, pp. 151–156, 1986.
10. Güneş, Y., “2023 BDTIM Earthquake and Explosion Evaluatıon Report”, 2023.

11. McKenzie, D., “Active Tectonics of the Mediterranean Region”, *Geophysical Journal International*, Vol. 30, No. 2, pp. 109–185,1972.

12. McKenzie, D., “The East Anatolian Fault: A major structure in Eastern Turkey”, *Earth and Planetary Science Letters*, Vol. 29, No. 1, pp. 189–193, 1976.

13. Dewey, J. F., M. R. Hempton, W. S. F. Kidd, F. Şaroğlu, and A. M. C. Şengör, “Shortening of continental lithosphere: The neotectonics of Eastern Anatolia - A young collision zone”, *Geological Society*, Vol. 19, No. 1, pp. 1–36, 1986.

14. Delph, J. R., C. B. Biryol, S. L. Beck, G. Zandt, and K. M. Ward, “Shear wave velocity structure of the Anatolian Plate: anomalously slow crust in southwestern Turkey”, *Geophysical Journal International*, Vol. 202, No. 1, pp. 261–276, 2015.

15. Jackson, J., “Active tectonics of the Aegean region”, *Annual Review of Earth and Planetary Sciences*, Vol. 22, pp. 239–271, 1994.

16. Le Pichon, X., N. Chamot-Rooke, S. Lallemant, R. Noomen, and G. Veis, “Geodetic determination of the kinematics of central Greece with respect to Europe: Implications for eastern Mediterranean tectonics”, *Journal of Geophysical Research Solid Earth*, Vol. 100, No. B7, pp. 12675–12690, 1995.

17. Şengör, A. M. C., and B. A. Natal, “Turkic-type orogeny and its role in the making of the continental crust”, *Annual Review of Earth and Planetary Sciences*, Vol. 24, pp. 263–337, 1996.

18. Ozer, C., M. Ozyazicioglu, E. Gok, and O. Polat, “Imaging the Crustal Structure Throughout the East Anatolian Fault Zone, Turkey, by Local Earthquake Tomography”, *Pure and Applied Geophysics*, Vol. 176, No. 6, pp. 2235–2261, 2019.

19. Aktug, B., H. Ozener, A. Dogru, A. Sabuncu, B. Turgut, K. Halicioglu, O. Yilmaz, and E. Havazli, “Slip rates and seismic potential on the East Anatolian Fault System using an improved GPS velocity field”, *Journal of Geodynamics*, Vol. 94–95, pp. 1–12, 2016.

20. Dolmaz, M. N., O. Elitok, and U. Y. Kalyoncuoglu, “Interpretation of low seismicity in the Eastern Anatolian Collisional zone using geophysical (Seismicity and Aeromagnetic) and geological data”, *Pure and Applied Geophysics*, Vol. 165, No. 2, pp. 311–330, 2008.

21. Hempton, M. R., “Constraints on Arabian Plate motion and extensional history of the Red Sea”, *Tectonics*, Vol. 6, No. 6, pp. 687–705, 1987.

22. Le Pichon, X., and C. Kreemer, “The miocene-to-present kinematic evolution of the eastern mediterranean and middle east and its implications for dynamics”, *Annual Review of Earth and Planetary Sciences,* Vol. 38, No. 1, pp. 323–351, 2010.

23. Duman, T. Y., and O. Emre, “The east anatolian fault: Geometry, segmentation and jog characteristics”, *Geological Society*, Vol. 372, No. 1, pp. 495–529, 2013.

24. Burke, K., and A. M. C. Sengor, “Tectonic escape in the evolution of the continental crust”, *Reflection Seismology: The Continental Crust Geodynamics Series*, pp. 41–53, 1986.

25. Nalbant, S. S., J. McCloskey, S. Steacy, and A. A. Barka, “Stress accumulation and increased seismic risk in Eastern Turkey”, *Earth and Planetary Science Letters*, Vol. 195, No. 3–4, pp. 291–298, 2002.

26. Vanacore, E. A., T. Taymaz, and E. Saygin, “Moho structure of the Anatolian Plate from receiver function analysis”, *Geophysical Journal International*, Vol. 193, No. 1, pp. 329–337, 2013.

27. Simão, N. M., S. S. Nalbant, F. Sunbul, and A. Komec Mutlu, “Central and eastern Anatolian crustal deformation rate and velocity fields derived from GPS and earthquake data”, *Earth and Planetary Science Letters*, Vol. 433, pp. 89–98, 2016.

28. Arpat, E., and F. Şaroğlu, “The East Anatolıan Fault System; Thoughts On Its Development”, *Bulletin of the Mineral Research and Exploration*, Vol. 78, pp. 33–39, 1972.

29. Arpat, E., and F. Şaroğlu, “Some recent tectonic events in Turkey”, *Geological Bulletin of Turkey*, Vol. 18, pp. 91–101, 1975.

30. Şaroğlu, F., Ö. Emre, and İ. Kuşçu, “The East Anatolian fault zone of Turkey”, *Annales Tectonicae*, Vol. 6, pp. 99–125, 1992.

31. Muehlberger, W. R., and M. B. Gordon, “Observations on the complexity of the East Anatolian Fault, Turkey”, *Journal of Structural Geology*, Vol. 9, No. 7, pp. 899–903, 1987.

32. Şengör A. M. C., N. Görür, and F. Şaroğlu, “Strike-slip faulting and related basin formation in zones of tectonic escape: Turkey as a case study”, *Society for Sedimentary Geology*, Vol. 37, pp. 227-264, 1985.

33. Şaroğlu, F., and Y. Yılmaz, “Geological Evolution and Basin Models During Neotectonic Episode in the Eastern Anatolia”, *Bulletin of the Mineral Research and Exploration*, Vol. 107, No. 107, pp. 70–93, 1986.

34. Ambraseys, N. N., “Temporary seismic quiescence: SE Turkey”, *Geophysical Journal International*, Vol. 96, No. 2, pp. 311–331, 1989.

35. Ambraseys, N. N., and J. A. Jackson, “Faulting associated with historical and recent earthquakes in the Eastern Mediterranean region”, *Geophysical Journal International*, Vol. 133, No. 2, pp. 390–406, 1998.

36. Konca A. Ö., H. Karabulut, S. E. Güvercin, F. Eskiköy, S. Özarpacı, A. Özdemir, M. Floyd, S. Ergintav, and U. Doğan, “From Interseismic Deformation With Near-Repeating Earthquakes to Co-Seismic Rupture: A Unified View of the 2020 Mw6.8 Sivrice (Elazığ) Eastern Turkey Earthquake”, *Journal of Geophysical Research: Solid Earth*, Vol. 126, No. 10, 2021.

37. Yurtmen, S., H. Guillou, R. Westaway, G. Rowbotham, and O. Tatar, “Rate of strike-slip motion on the Amanos Fault (Karasu Valley, southern Turkey) constrained by K–Ar dating and geochemical analysis of Quaternary basalts”, *Tectonophysics*, Vol. 344, No. 3–4, pp. 207–246, 2002.

38. Seyrek A., T. Demir, M. S. Pringle, S. Yurtmen, R. W. C. Westaway, A. Beck, and G. Rowbotham, “Kinematics of the Amanos Fault, southern Turkey, from

Ar/Ar dating of offset Pleistocene basalt flows: Transpression between the African and Arabian plates", *Geological Society*, Vol. 290, pp. 255–284, 2007.

39. Taymaz, T., A. Ganas, S. Yolsal-Cevikbilen, F. Vera, T. Eken, C. Erman, D. Keleş, V. Kapetanidis, S. Valkaniotis, I. Karasante, V. Tsironi, P. Gaebler, D. Melgar, and T. Ocalan, "Source Mechanism and Rupture Process of the 24 January 2020 Mw 6.7 Doğanyol–Sivrice Earthquake obtained from Seismological Waveform Analysis and Space Geodetic Observations on the East Anatolian Fault Zone (Turkey)", *Tectonophysics*, Vol. 804, No. 3, 2021.

40. Yolsal-Çevikbilen, S., T. Taymaz, T. S. Irmak, C. Erman, M. Kahraman, B. Özkan, T. Eken, T. Öcalan, A. H. Doğan, and C. Altuntaş, "Source Geometry and Rupture Characteristics of the 20 February 2023 Mw 6.4 Hatay (Türkiye) Earthquake at Southwest Edge of the East Anatolian Fault", *Geochemistry, Geophysics, Geosystems*, Vol. 25, No. 10, 2024.

41. Kanamori, H., and D. L. Anderson, "Theoretical basis of some empirical relations in seismology", *Bulletin of the Seismological Society of America*, Vol. 65, No. 5, pp. 1073–1095, 1975.

42. Miyake, H., T. Iwata, and K. Irikura, "Source Characterization for Broadband Ground-Motion Simulation: Kinematic Heterogeneous Source Model and Strong Motion Generation Area", *Bulletin of the Seismological Society of America*, Vol. 93, No. 6, pp. 2531–2545, 2003.

43. Somerville, P., K. Irikura, R. Graves, S. Sawada, D. Wald, Y. Iwasaki,T. Kagawa, N. Smith, and A. Kowada, "Characterizing crustal earthquake slip models for the prediction of strong ground motion", *Seismological Research Letters*, Vol. 70, No. 1, pp. 59–80, 1999.

44. Mendoza, C., and S. H. Hartzell, "Inversion for slip distribution using teleseismic P waveforms: North Palm Springs, Borah Peak, and Michoacan earthquakes", *Bulletin of the Seismological Society of America*, Vol. 78, No. 3, pp. 1092–1111, 1988.

45. Hutchings, L., "'Prediction' of Strong Ground Motion for the 1989 Loma Prieta Earthquake using Empirical Green's Functions," *Bulletin of the Seismological Society of America*, Vol. 81, No. 5, pp. 1813–1837, 1991.

46. Mai, P. M., and G. C. Beroza, "A spatial random field model to characterize complexity in earthquake slip", *Journal of Geophysical Research: Solid Earth*, Vol. 107, No. B11, pp. ESE 10-1, 2002.

47. Mai, P. M., and G. C. Beroza, "Source Scaling Properties from Finite-Fault-Rupture Models", *Bulletin of the Seismological Society of America*, Vol. 90, No. 3, pp. 604–615, 2000.

48. Houshmandviki, A., H. Hamzehloo, H. Miyake, and A. Ansari, "Estimation of Strong Motion Generation Area for the 2004 Parkfield Earthquake Using Empirical Green's Function Method", *Pure and Applied Geophysics*, Vol. 177, pp. 2241–2254, 2020.

49. Custódio, S., P. Liu, and R. J. Archuleta, "The 2004 Mw6.0 Parkfield, California, earthquake: Inversion of near-source ground motion using multiple data sets", *Geophysical Research Letters*, Vol. 32, No. 23, pp. 1–4, 2005.

50. Chen J. [Caltech], "Slip history the 2004 (Mw 5.9) Parkfield Earthquake (Single-Plane Model)", 2004, http://www.tectonics.caltech.edu/slip_history /2004 _ca/parkfield2.html, last accessed January 21, 2025.

51. Irikura, K., K. Miyakoshi, K. Kamae, K. Yoshida, K. Somei, S. Kurahashi, and H. Miyake, "Applicability of source scaling relations for crustal earthquakes to estimation of the ground motions of the 2016 Kumamoto earthquake", *Earth, Planets and Space*, Vol. 69, No. 10, 2017.

52. Yoshida, K., K. Miyakoshi, K. Somei, and K. Irikura, "Source process of the 2016 Kumamoto earthquake (Mj7.3) inferred from kinematic inversion of strong-motion records", *Earth, Planets and Space*, Vol. 69, No. 64, 2017.

53. Asano, K., and T. Iwata, "Source rupture processes of the foreshock and mainshock in the 2016 Kumamoto earthquake sequence estimated from the kinematic waveform inversion of strong motion data", *Earth, Planets and Space*, Vol. 68, No. 147, 2016.

54. Kubo, H., W. Suzuki, S. Aoi, and H. Sekiguchi, “Source rupture processes of the 2016 Kumamoto, Japan, earthquakes estimated from strong-motion waveforms”, *Earth, Planets and Space*, Vol. 68, No. 161, 2016.

55. Miyake, H., T. Iwata, and K. Irikura, “Strong Ground Motion Simulation and Source Modeling of the Kagoshima-ken Hokuseibu Earthquakes of March 26 (MJMA6.5) and May 13(MJMA6.3), 1997, Using Empirical Green’s Function Method”, *Journal of the Seismological Society of Japan*, Vol. 51, No. 4, pp. 431–442, 1999.

56. Irikura, K., and H. Miyake, “Recipe for predicting strong ground motion from crustal earthquake scenarios”, *Pure and Applied Geophysics*, Vol. 168, No. 1–2, pp. 85–104, 2011.

57. Yoshida, S., K. Koketsu, B. Shibazaki, T. Sagiya, T. Kato, and Y. Yoshida, “Joint Inversion of Near-and Far-field Waveforms and Geodetic Data for the Rupture Process of the 1995 Kobe Earthquake”, *Journal of Physics of the Earth*, Vol. 44, No. 5, pp. 437–454, 1996.

58. Kobayashi, R., S. Miyazaki, and K. Koketsu, “Source processes of the 2005 West Off Fukuoka Prefecture earthquake and its largest aftershock inferred from strong motion and 1-Hz GPS data”, *Earth, Planets and Space*, Vol. 58, pp. 57–62, 2006.

59. Birgören, G., H. Sekiguchi, and K. Irikura, “Rupture model of the 1999 Düzce, Turkey, earthquake deduced from high and low frequency strong motion data”, *Geophysical Research Letters*, Vol. 31, No. 5, 2004.

60. Tanırcan, G., and N. Savaş, “Strong ground motion simulation by the Empirical Green’s Function method for Bursa-Yalova Region, Turkey”, *Bulletin of Earthquake Engineering*, Vol. 9, No. 5, pp. 1327–1338, 2011.

61. Baykal, M., H. Miyake, and T. Yokoi, “Source Model of the 2010 Elazığ Kovancılar Earthquake (Mw 6.1) for Broadband Ground Motion Simulation”, *15th World conference on earthquake engineering (15WCEE)*, Lisboa, Portugal, 2012.

62. Tanırcan, G., H. Miyake, H. Yamanaka, and O. Özel, “Large Stress Release During Normal-Faulting Earthquakes in Western Turkey Supported by Broadband Ground Motion Simulations”, *Pure and Applied Geophysics*, Vol. 177, No. 4, pp. 1969–1981, 2020.

63. Hanks, T. C., and H. Kanamori, “A moment magnitude scale”, *Journal of Geophysical Research: Solid Earth*, Vol. 84, No. B5, pp. 2348–2350, 1979.

64. Kadirioğlu, F. T., and R. F. Kartal, “The new empirical magnitude conversion relations using an improved earthquake catalogue for Turkey and its near vicinity (1900-2012)”, *Turkish Journal of Earth Sciences*, Vol. 25, No. 4, pp. 300–310, 2016.

65. Akyuz, H. S., E. Altunel, V. Karabacak, and C. C. Yalciner, “Historical earthquake activity of the northern part of the Dead Sea Fault Zone, southern Turkey”, *Tectonophysics*, Vol. 426, No. 3–4, pp. 281–293, 2006.

66. Shearer, P. M., R. E. Abercrombie, D. T. Trugman, and W. Wang, “Comparing EGF Methods for Estimating Corner Frequency and Stress Drop From P Wave Spectra”, *Journal of Geophysical Research: Solid Earth*, Vol. 124, No. 4, pp. 3966–3986, 2019.

67. Wu, Q., M. Chapman, and X. Chen, “Stress-Drop Variations of Induced Earthquakes in Oklahoma”, *Bulletin of the Seismological Society of America*, Vol. 108, No. 3A, pp. 1107–1123, 2018.

68. Abercrombie, R. E., “Investigating uncertainties in empirical green’s function analysis of earthquake source parameters”, *Journal of Geophysical Research: Solid Earth*, Vol. 120, No. 6, pp. 4263–4277, 2015.

69. Brune, J. N., “Correction [to ‘Tectonic stress and the spectra, of seismic shear waves from earthquakes’]”, *Journal of Geophysical Research*, Vol. 76, No. 20, pp. 5002–5002, 1971.

70. *Technical Standards and Commentaries for Port and Harbour Facilities in Japan*, 2020.

71. Aki, K., “Scaling law of seismic spectrum”, *Journal of Geophysical Research*, Vol. 72, No. 4, pp. 1217–1231, 1967.

72. Boore, D. M., “Simulation of Ground Motion Using the Stochastic Method”, *Pure and Applied Geophysics*, Vol. 160, No. 3, pp. 635–676, 2003.

73. Lay, T., and T. C. Wallace, “Modern Global Seimology”, *International geophysics series*, Vol. 58, 1995.

74. Aki, K., “Attenuation of shear-waves in the lithosphere for frequencies from 0.05 to 25 Hz”, *Physics of the Earth and Planetary Interiors*, Vol. 21, No. 1, pp. 50–60, 1980.

75. Boore, D. M., “Use of seismoscope records to determine ML and peak velocities”, *Bulletin of the Seismological Society of America*, Vol. 74, No. 1, pp. 315–324, 1984.

76. Raghukanth, S. T. G., and S. N. Somala, “Modeling of strong-motion data in Northeastern India: Q, stress drop, and site amplification”, *Bulletin of the Seismological Society of America*, Vol. 99, No. 2A, pp. 705–725, 2009.

77. Motazedian, D., “Region-specific key seismic parameters for earthquakes in northern Iran”, *Bulletin of the Seismological Society of America*, Vol. 96, No. 4A, pp. 1383–1395, 2006.

78. Haskell, N. A., “Crustal reflection of plane SH waves”, *Journal of Geophysical Research*, Vol. 65, No. 12, pp. 4147–4150, 1960.

79. Sanchez-Sesma, F. J., “Site effects on strong ground motion”, *Soil Dynamics and Earthquake Engineering*, Vol. 6, No. 2, pp. 124–132, 1987.

80. Pitarka, A., K. Irikura, T. Iwata, and H. Sekiguchi, “Three-dimensional simulation of the near-fault ground motion for the 1995 Hyogo-Ken Nanbu (Kobe), Japan, earthquake”, *Bulletin of the Seismological Society of America*, Vol. 88, No. 2, pp. 428–440, 1998.

81. Boore, D. M., and W. B. Joyner, “Site amplifications for generic rock sites”, *Bulletin of the Seismological Society of America*, Vol. 87, No. 2, pp. 327–341, 1997.

82. Hanks, T. C., “fmax”, *Bulletin of the Seismological Society of America*, Vol. 72, No. 6A, pp. 1867–1879, 1982.

83. Papageorgiou, A. S., and K. Aki, “A specific barrier model for the quantitative description of inhomogeneous faulting and the prediction of strong ground motion. Part II. Applications of the model”, *Bulletin of the Seismological Society of America*, Vol. 73, No. 4, pp. 953–978, 1983.

84. Anderson, J. G., and S. E. Hough, “A model for the shape of the fourier amplitude spectrum of acceleration at high frequencies”, *Bulletin of the Seismological Society of America*, Vol. 74, No. 5, pp. 1969–1993, 1984.

85. Havskov, J., and L. Ottemoller, *Routine data processing in earthquake seismology: With sample data, exercises and software*, New York, 2010.

86. Hanks, T. C., and R. K. McGuire, “The character of high-frequency strong ground motion”, *Bulletin of the Seismological Society of America*, Vol. 71, No. 6, pp. 2071–2095, 1981.

87. Kamae, K., and K. Irikura, “Source model of the 1995 Hyogo-Ken Nanbu earthquake and simulation of near-source ground motion”, *Bulletin of the Seismological Society of America*, Vol. 88, No. 2, pp. 400–412, 1998.

88. Kanamori, H., “A semi-empirical approach to prediction of long-period ground motions from great earthquakes”, *Bulletin of the Seismological Society of America*, Vol. 69, No. 6, pp. 1645–1670, 1979.

89. Dan, K., T. Watanabe, and T. Tanaka, “A Semi-Empirical Method to Synthesize Earthquake Ground Motions Based on Approximate Far-Field Shear-Wave Displacement”, *Journal of Structural and Construction Engineering (Transactions of AIJ)*, Vol. 396, pp. 27–36, 1989.

90. Irikura, K., and K. Kamae, “Estimation of strong ground motion in broad-frequency band based on a seismic source scaling model and an empirical Green’s function technique”, *Annals of Geophysics*, Vol. 37, No. 6, 1994.

91. K. Irikura, H. Sekiguchi, and T. Kagawa, “Revision of the empirical Green’s function method”, *Seismological Society of Japan*, Vol. 2, No. B25, 1997.

92. Cheloni D., and A. Akinci, “Source modelling and strong ground motion simulations for the 24 January 2020, Mw 6.8 Elazığ earthquake, Turkey”, *Geophysical Journal International*, Vol. 223, No. 2, pp. 1054–1068, 2020.

93. Olsen, K. B., and J. E. Mayhew, “Goodness-of-fit criteria for broadband synthetic seismograms, with application to the 2008 Mw 5.4 Chino Hills, California, Earthquake”, *Seismological Research Letters*, Vol. 81, No. 5, pp. 715–723, 2010.

94. Dragovich, J. J., and A. Lepage, “FDE index for goodness-of-fit between measured and calculated response signals”, *Earthquake Engineering & Structural Dynamics*, Vol. 38, No. 15, pp. 1751–1758, 2009.

95. Bielak, J., R. W. Graves, K. B. Olsen, R. Taborda, L. Ramírez-Guzmán, S. M. Day, G. P. Ely, D. Roten, T. H. Jordan, P. J. Maechling, J. Urbanic, Y. Cui, and G. Juve, “The ShakeOut earthquake scenario: Verification of three simulation sets”, *Geophysical Journal International*, Vol. 180, No. 1, pp. 375–404, 2010.

96. Smerzini, C., M. Vanini, R. Paolucci, P. Renault, and P. Traversa, “Regional physics-based simulation of ground motion within the Rhône Valley, France, during the MW 4.9 2019 Le Teil earthquake”, *Bulletin of Earthquake Engineering*, Vol. 21, No. 4, pp. 1747–1774, 2023.

97. Kristeková, M., J. Kristek, P. Moczo, and S. M. Day, “Misfit criteria for quantitative comparison of seismograms”, *Bulletin of the Seismological Society of America*, Vol. 96, No. 5, pp. 1836–1850, 2006.

98. Karimzadeh, S., “Seismological and Engineering Demand Misfits for Evaluating Simulated Ground Motion Records”, *Applied Sciences*, Vol. 9, No. 21, pp. 4497, 2019.

99. Anderson, J. G., “Quantitative measure of the goodness-of-fit of synthetic seismograms”, *13th World Conference on Earthquake Engineering,* Vancouver, Canada, No. 243, 2024.

100. Arias, A., “MEASURE OF EARTHQUAKE INTENSITY.”, *Seismic Design for Nuclear Power Plants*, pp. 438–483, 1970.

101. Wu, Y. M., T. liang Teng, T. C. Shin, and N. C. Hsiao, “Relationship between peak ground acceleration, peak ground velocity, and intensity in Taiwan”, *Bulletin of the Seismological Society of America*, Vol. 93, No. 1, pp. 386–396, 2003.

102. Hall, J. F., T. H. Heaton, M. W. Halling, and D. J. Wald, “Near-Source Ground Motion and its Effects on Flexible Buildings”, *Earthquake Spectra*, Vol. 11, No. 4, pp. 569–605, 1995.

103. Bray, J. D., and T. Travasarou, “Simplified Procedure for Estimating Earthquake-Induced Deviatoric Slope Displacements”, *Journal of Geotechnical and Geoenvironmental Engineering*, Vol. 133, No. 4, pp. 381–392, 2007.

104. Power, M., B. Chiou, N. Abrahamson, Y. Bozorgnia, T. Shantz, and C. Roblee, “An Overview of the NGA Project”, *Earthquake Spectra*, Vol. 24, No. 1, pp. 3–21, 2008.

105. Sokolov, V. Y., and Y. K. Chernov, “On the correlation of seismic intensity with fourier amplitude spectra”, *Earthquake Spectra*, Vol. 14, No. 4, pp. 679–694, 1998.

106. Wells, D. L., and K. J. Coppersmith, “New empirical relationships among magnitude, rupture length, rupture width, rupture area, and surface displacement”, *Bulletin - Seismological Society of America*, Vol. 84, No. 4, pp. 974–1002, 1994.

107. Kuran, F., G. Tanırcan, and E. Pashaei, “Developing machine learning-based ground motion models to predict peak ground velocity in Turkiye”, *Journal of Seismology*, Vol. 28, No. 5, pp. 1183–1204, 2024.

108. Sandıkkaya, M. A., B. Güryuva, Ö. Kale, O. S. Okçu, A. İçen, E. Yenier, and S. Akkar,, “An updated strong-motion database of Türkiye (SMD-TR)”, *Earthquake Spectra*, Vol. 40, No. 1, pp. 847–870, 2024.

109. Barbot, S., H. Luo, T. Wang, Y. Hamiel, O. Piatibratova, M. Javed, C.Braitenberg, and G.Gürbüz, “Slip distribution of the February 6, 2023 Mw

7.8 and Mw 7.6, Kahramanmaraş, Turkey earthquake sequence in the East Anatolian Fault Zone", *Seismica*, Vol. 2, No. 3, 2023.

110. Batman, O., S. Akbaşak, B. S. Demirtaş, and G. Tanırcan, "Source Parameters of the 2023 Kahramanmaraş Earthquake Aftershocks in the East Anatolian Fault Zone", *Proceedings of the 7th International Conference on Earthquake Engineering and Seismology*, Antalya, Turkiye, Vol. 2, pp. 71–85, 2024.